Construction of a Scintillator Fiber Detector for Space Applications

Bachelor Thesis

Sabrina Kressierer

04. November 2020

Prof. Dr. Laura Fabietti
Dense and Strange Hadronic Matter Group — Physik-Department E62
Technische Universität München

Supervisor and primary reviewer: Prof. Dr. Laura Fabietti
Advisor: Stephan Königstorfer

Abstract

Scintillator fiber particle detectors using Bragg curve spectroscopy allow for particle identification at relatively easy maintenance and compact sizes. By using a special crossed layers configuration, these detectors can measure three dimensional spacial and energetic resolution in a cube of just 10x10x10 cm. This detector can differentiate between particle and anti-particle over a range of 25 up to several hundred MeV per nucleon. These properties make it ideal for space applications, and thus the development of such detectors is the focus of this bachelor thesis. Hence, the special feature of the detector core, the 90° rotating layers with plastic fibers, and the production of these - in total - 1024 plastic fibers is discussed. Subsequently, the produced fibers are characterized. For the first quality control, measurements with Strontium are implemented. They lead to a total standard deviation of $\sigma_{total} = 13\%$. Furthermore, the electronic readout, which is done with the Time-over-Threshold-Method, is treated in this thesis. Various measurements which give, among others, information about resolution, crosstalk, and noise are described. Finally, a beamtime at a pion and proton beamline at the Paul-Scherrer-Institute (PSI) serves as a functionality check. This thesis encloses a first rough analysis and calibration of the measured data.

Contents

Chapter 1

Introduction

1.1 Overview

For mankind, space travel has always been a journey into the unknown. Even though our knowledge about the cosmos matures daily, there are still countless gaps in our knowledge that one needs to fill. This necessitates not only theoretical considerations but also the approprate measuring devices. This bachelor thesis is about constructing a detector that should make it possible to obtain further knowledge about cosmic radiation. However, the focus is on pursuing new discoveries and replacing the existing measuring instruments with a simpler and more compact design and hence should facilitate access to research results. This work focuses on the detector's unique design, allowing for analyzing a particle's three-dimensional trajectory and identifying it.

Furthermore, the production of the required components and their quality control is explained. The finished detector modules are subjected to extensive tests regarding their electronic readout to finally examine them for their functionality check during a beamtime at the PSI (Paul Scherrer Institute).

1.2 Cosmic Rays

Cosmic rays are high-energy particles, mainly protons, arriving from outer space to Earth, where they hit the atoms in the upper atmosphere and create new particles, mainly pions. The energies of the primary cosmic rays range from around 1 GeV to as much as 100 EeV[1]. [1] The flux of the cosmic rays can be seen in figure 1.2. The

[1]Exa-electronvolt 10^{18}

spectrum[2] is separated into three parts. At an energy of around 3PeV[3], there is a break called the "knee"; cosmic rays up to this energy are Galactic rays. Cosmic rays with energies above the "ankle" are described as extragalactic rays with energies beyond 100 EeV. [3] Cosmic Rays consists of ∼98% nuclei and ∼2% electrons and positrons, while the nuclei are composed of ∼87% hydrogen, ∼12% helium and ∼1% for all heavier nuclei [4, p.330]. The origin of cosmic rays is still unknown. Challenges are determining the exact spectra of hydrogen and helium, the main components of cosmic rays, and the fraction of anti-particles' energy dependence. [2] This incomplete knowledge, which has received increased attention for space missions, especially for deep-space-flights such as Moon or Mars flights with no relevant protection by magnetospheres or atmospheres. Reliable monitoring of the radiation environment of astronauts is heavily related to a profound understanding of cosmic rays. [5] With our detector, we want to measure protons and completely ionized (heavy) atoms up to $^{56}_{26}$Fe.

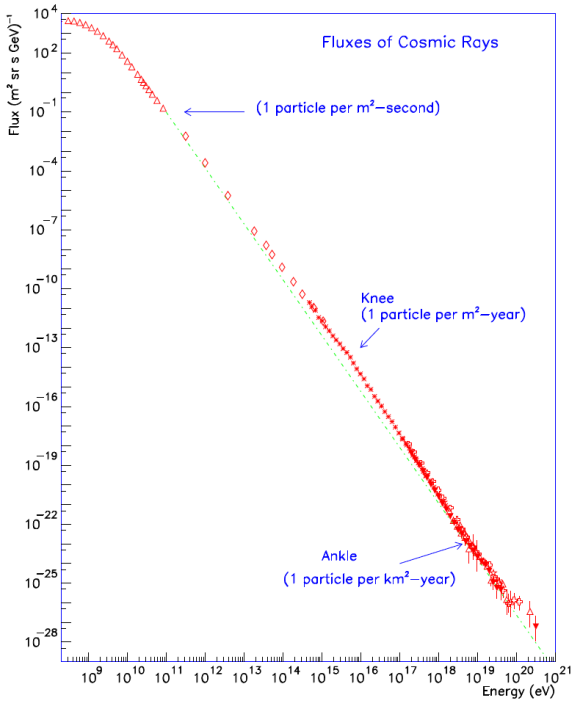

Figure 1.1: Spectrum of cosmic rays. [6]

[2]The number of particles at a certain energy E within a certain small energy interval dE is called the spectrum. [2]

[3]Peta-electronvolt 10^{15}

1.3 Measurement Methods

There are different types of detectors that are usually used for radiation measurements in space. Dosimeters provide information about the total ionizing dose omnidirectionally but obtain no data about the particle characteristics like energy or incidence angle. For energy measurements, a calorimeter, and for particle identification, a Cherenkov detector can be used. [7] A calorimeter can measure the total energy of a particle. If a charged particle has a velocity higher than the light velocity in a medium, it leads to light emission. As a threshhold indicator a Cherenkov detector can detect these particles [8]. These are typically components of particle telescopes, which have the disadvantage of a limited field of view. A better particle identification can be reached with spectrometers, where a magnetic field is added, but this leads to a higher weight of the system. So the project of our scintillation fiber detector for space application deals with the challenge of combining the advantages of these different types and finally constructing one detector, that can measure particle fluxes omnidirectionally, the particles' energies, and identify them. [7]

Chapter 2

Theory

2.1 Light Detectors and Scintillation

The principle of scintillation for detecting ionizing particles is to convert the light generated from the incident radiation energy into an electrical pulse. Scintillation is the process by which a charged particle hits the scintillating material and thereby loses kinetic energy. This process creates excited electrons that decay, and thus emit light. Two important requirements have to be fulfilled to get an ideal scintillation material. First, the decay time should be short to increase temporal resolution. Further, the material should convert the kinetic energy of charged particles into detectable light with a high scintillation efficiency, ideally linear, so that the light yield is proportional to the deposited energy. One has to differentiate between inorganic and organic scintillators, since most inorganics have a higher light output, while organics are faster in their response time. [9, p.219-220]

Inorganic scintillators have a crystalline structure. For the scintillating process, the energy states of the electrons in the crystal grids are relevant. When electrons from the valence band are elevated to the conduction band because of an excitation, electron-hole-pairs are created. Inorganic scintillators have a high density and a high mass of their constituent atoms, making them particularly useful for detecting photons in gamma-ray spectroscopy. [10]

Organic materials are plastics or liquid solutions. They usually consist of a solvent and a scintillator. Energy is released by an ionizing particle and flows to the scintillator. The light emitted by the scintillator is absorbed and re-emitted. [11] Solutions of organics can be a relatively inexpensive option, while also exhibiting the best radiation hardness. These solutions can be polymerized to produce them in many shapes, which makes them easy to handle. [10]

For the detector's construction, this thesis is about one of the most common organic scintillators applications: scintillating plastic fibers. They are typically based on polystyrene. The fibers have a scintillating core and a thin surrounding layer of cladding material, protecting the core from surface abrasion and accumulation of foreign material. The light is transported through the fiber by total reflection. Since the light output of fibers is relatively low, the light sensors should have low intrinsic noise and reasonable resolution for low photon counts. [10] Scintillating plastic fibers have a linear response to the deposited energy for small and a non-linear response for higher energies. It should be mentioned, that this effect is called "quenching" [5]. However, a discussion of the this effect exceeds the scope of this thesis. The structure of such a plastic fiber and the process of light transport can be seen in figure 2.1. For this project, we purchased scintillating plastic fibers from the company kuraray [12]. The used type of fibers is called SCSF-78 which is characteristic of a long attenuation length and a high light yield. The decay time is 2.8ns. The treatment process of these fibers will be explained in section 4.1.

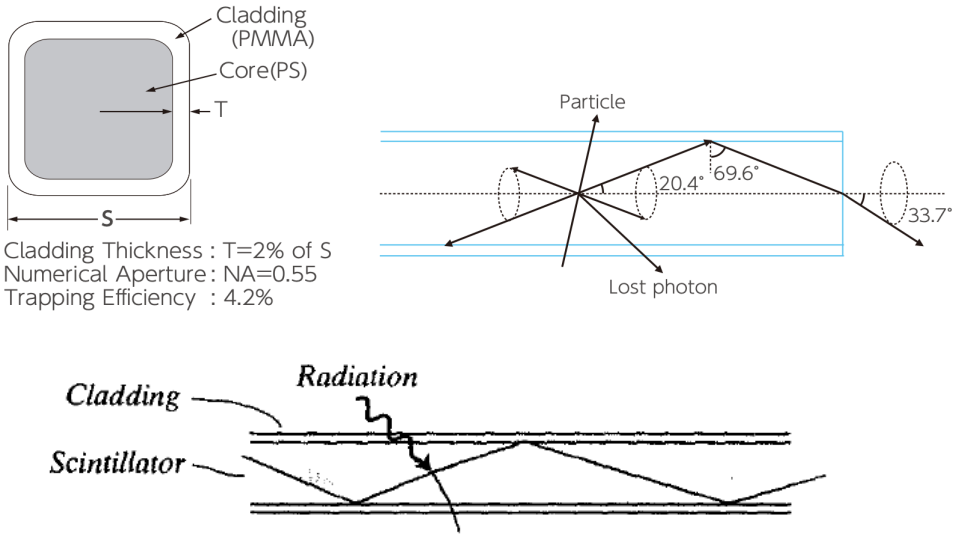

Figure 2.1: Working principle of a scintillating plastic fiber. The used fibers have a length of 80mm and a thickness of 2mm. The cladding material is polymethylmethacrylate. The light transport takes place via total reflection [9]; [12]

2.2 Photmultiplier Tube

A photomultiplier (PM) converts the light output of a scintillation pulse into an electrical signal. The PM tube components have a vacuum enclosure, so low-energy electrons can be accelerated efficiently by internal electric fields without being deflected. The process can be separated into three steps:

1. The absorption of the incident photon and transfer of energy to an electron within the photoemissive material

2. The acceleration of that electron towards the photoanode

3. Multiplication of the electrons

For this, there are two main components (to be seen in figure 2.2). The photocathode, a photosensitive layer, is coupled to an electron multiplier structure. It is responsible for converting the incoming light photons into low-energy electrons. The electron multiplier section in a PM tube is a nearly ideal amplifier to increase the photoelectrons. After this amplification, there are sufficient electrons to be detected and serve as the charge signal. This charge is collected at the anode or output stage of the multiplier structure. [9, p.265f]

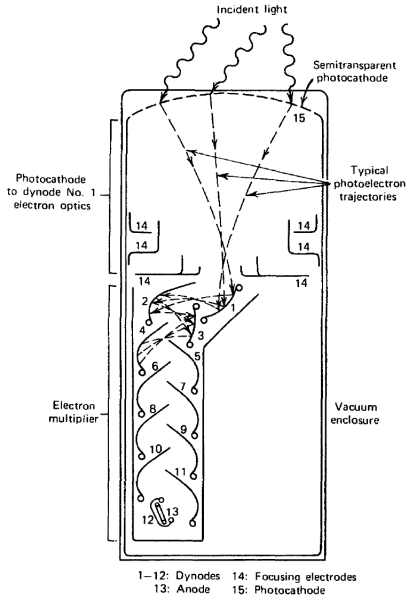

Figure 2.2: Two main components of a PM tube [9]

2.3 Principles of solid-state Photodetectors

In solids (crystals), the electron energy levels are split in bands (figure 2.3). An excited electron of the valence band can be exited into the conduction band due to a process with energy transfer, which means, in general, either a thermal process or a process with incident photons. This process creates a hole in the valence band. [13] In a semiconductor, these holes and electrons are responsible for current flow. This current can be influenced by the introduction of foreign atoms (doping). The density of electrons is named n, the density for holes p. If there are more electrons than holes, it is called an n-type conductor, otherwise a p-type conductor. [14] Connecting p and n forms a (PN-)diode (figure 2.4). At the p-n junction the charges are depleted, which leads to a zone free of charge carriers produced by an ionizing particle. A particle created by an incident photon drifts in the electric field and creates an electrical signal. [13]

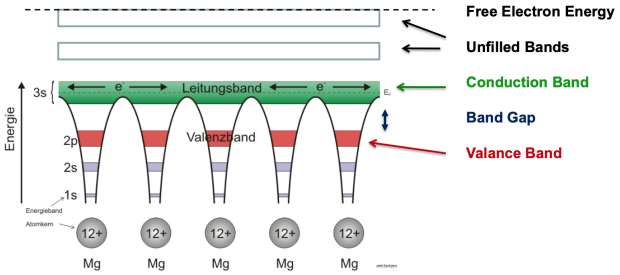

Figure 2.3: Energy bands ins solids [13]

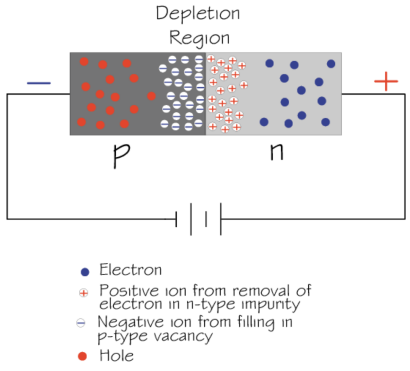

Figure 2.4: PN-Diode [13]

A PIN photodiode is a very simple and compact photodiode without the need for high operation voltages. It is an intrinsic piece of a semiconductor that is between two heavily doped n and p regions. The intrinsic region causes a very high reverse voltage, while the n and p regions lead to high currents in the forward direction. This configuration produces a field, separating the charges produced in the depleted region. The separated charges will be transferred to the terminals and detected as current. They were one of the first applications of silicon sensors for low light level detection and were developed to replace photomultipliers in high energy physics experiments. The most common material is silicon. [15] For our detector we used Silicon photomultipliers (SiPms), from the company KETEK GmbH[1] as well. They are based on PN-Diodes.

To get the information about the primary particle's energy that caused the light flash, the signals' amplitude needs to be analyzed event by event. For this, the SiPMs were developed, arrays of Avalanche Photodiodes (APD's), which operate in Geiger-Mode, also known as Geiger-Mode Avalanche Photodiodes (G-APD). In an APD, a photoelectron in the electric field gains enough energy to create an electron-hole pair by impact ionization. The initial electron as well as the additional electrons can create an avalanche, are then accelerated, and thus create more and more electron-hole pairs. [15] Operation in Geiger-Mode means that one set an (over-)voltage, so the APD breaks down when the signal is coming. That leads to a massive discharge current, regardless of how many electrons were created. So a G-APD can detect single photons just like a Photomultiplier Tube with a very high gain. [16] The device configuration of a SiPm is divided into many cells that are connected parallel via an individual limiting resistor (figure 2.5) [15].

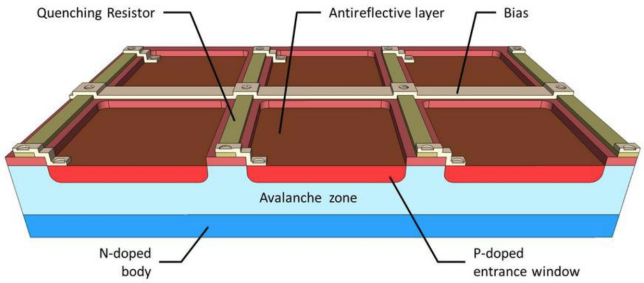

Figure 2.5: Structure of a SiPM based on a P-on-N structure. [17]

[1] https://www.ketek.net

2.4 Bragg Curve Spectroscopy

The particle identification for this detector is done via Bragg Curve Spectroscopy. The following formular has to be considered:

$$S = -\frac{dE}{dx} \tag{2.1}$$

where S is the linear stopping power for charged particles and $-\frac{dE}{dx}$ is also called the specific energy loss or the rate of teh energy loss. [9, p.31] If a charged particle goes through matter, the Bethe-Bloch-Formula describes the energy loss of this ionizing radiation:

$$\frac{dE}{dx} \sim z^2 \frac{Z}{A} \frac{1}{\beta^2} [ln(\gamma^2 \beta^2) - \beta^2] \tag{2.2}$$

where z is the charge of the incident particle, Z the atomic charge, A the mass of the absorbing material, β the speed of the incident particle and γ the Lorentz factor. One can see that the energy loss increases for decreasing kinetic energy. [10] Further, the higher the charge the higher the energy loss. This dependency is shwon in figure 2.6. [9, p.31]

It is also remarkable that, at about several hundred MeV, the specific energy loss approaches a constant value. Relativistic particles with a similar energy loss in this field are called minimum ionizing particles (MIPS). For low particle energies, the Bethe-Bloch-Formula becomes inexact. [9, p.31-32].

The Bragg Curve is defined as the plot of the specific energy loss over the distance traveled by a charged particle in the material. [9, p.32] A typically curve can be seen in figure 2.4. From the Bragg Curve, four measurement points can be determined: the total kinetic energy from the area under the curve, the maximum energy loss from the peak, the specific energy loss per distance from the length of the track, and the particle charge from the start of the curve. The Bragg peak is only related to the charge (the atomic number Z). With these four measurement points, one can identify the stopped particle. This evaluation process is called Bragg Curve Spectroscopy. [18, p.1]. With our detector, the energy loss per distance is not measured directly. Instead, the deposited energy per distance in the scintillation material (the plastic fibers) is calculated. The deceleration power and the length of the track results in the signal amplitude of the fiber. [7, p. 2]

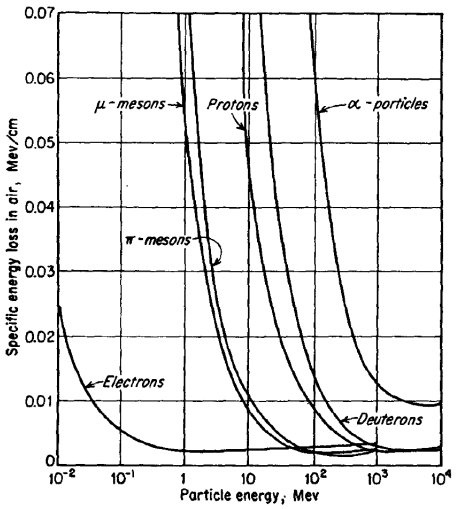

Figure 2.6: Variation of the specific energy loss in air versus energy of the charged particles shown [9]

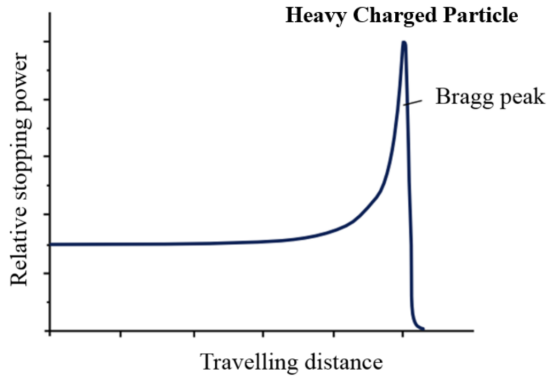

Figure 2.7: Sample Plot of a typical Break Curve [19]

Chapter 3

Detector Design

3.1 The RadMap Telescope

In section 1.3 the requirements of a multi-functional detector were explained. For this, the RadMap Telescope is being developed. The special characteristic of the RadMap Telescope is the combination of many features of the required devices in one single detector. It can measure the individual particle energy and direction quasi-omnidirectionally and differentiate them into particle and anti-particle over a range of 25 up to several hundred MeV per nucleon. One can not identify particles with higher energies, but it is possible to determine their total ionizing dose by calculating their energy loss. [5, 10] Additionally, the RadMap Telescope is very compact and fits in a cubic system with an edge length of only 10cm. It has a weight of less than 3.5kg and a low power consumption of about 30W. The advantage of this small configuration is that the detector is wearable for astronauts, which can also be used as a personal dosimeter with real-time measurements. [5, 10]

3.1.1 Construction

Five sensors build up the detector. The primary sensor is the Active Detection Unit (ADU) and is responsible for tracking and identifying the charged particles. The construction part of this thesis relates only to the ADU, but for completeness, the other components are explained shortly. Dosage and dosage rate measurements are quantified by two silicon sensors and two crystal dosimeters. The Central Control Unit (CCU) monitors the sensors, handles the data, and includes the digital devices. The parts are connected via a Controller Area Network (CAN) and a Peripheral Component Interconnect Express (PCIe) bus. A schematic overview is shown in figure 3.1. [5]

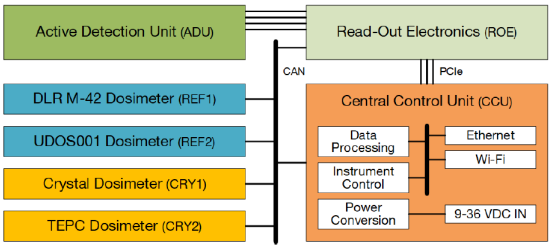

Figure 3.1: Arrangment of the main components of the detector [5]

3.1.2 Active Detection Unit (ADU)

The ADU, the detector's core, contains four modules that are stacked one above the other. In the following text, these modules will be called "the stacks." In total they include 1024 scintillating plastic fibers (section 2.1). The scintillating light is read out with SiPMs (section 2.3) and the determination takes place with Bragg Curve Spectroscopy (Section 2.4). [5] The special feature of the ADU is the 90° rotating layers, each with 32 fibers, which are arranged alternately. This configuration makes it possible to reconstruct the particle's three-dimensional trajectory. With this information and knowledge about the energy loss of the particles, they can be identified completely. [7, 10] The basic configuration of the ADU can be seen in figure 3.2.

In the following chapter, the scintillating plastic fibers' production and composition with the stacks will be explained in detail.

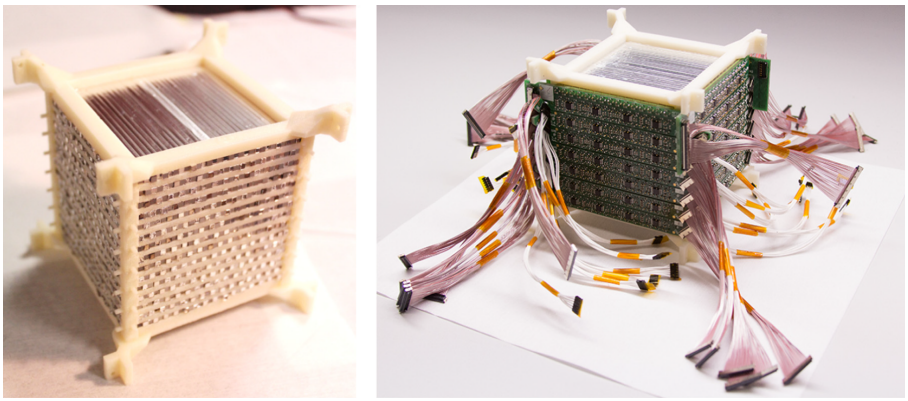

Figure 3.2: Old prototype of the ADU. Left: without SiPms. Right: with SiPms. [7] In contrast to this prototype, where all fibers are located in one module, the new prototype uses four independent modules. This arrangment will be shown in section 4.1.

Chapter 4

Production

4.1 Fiber Production

As in section 3.1 described, for the detector construction 1024 scintillating plastic fibers (section 2.1) had to be installed. The production took place in a cleanroom. The fibers had to be of a size of 80mm length, 2mm width, and 2mm depth. To get these forms, they were cut with pliers off a few meters roll of scintillating material. This raw material was purchased from the company kuraray [12]. The fibers' bent shape due to the roll's storage was eliminated by strongly fixing the fibers between two metal plates. Subsequently, the fixed fibers were baked in an oven. The determination of the baking process's duration, the temperature, and the time for the cool down process were part of a previous bachelor thesis[1] and thus will not be described in this context. Before and after the baking process, the fibers had to be cleaned carefully with isopropanol. Since the fibers were cut very roughly, one had to polish the ends of the fibers. Therefore, about 250 baked and cleaned fibers were put together in mounts specially designed for this process. The polishing procedure was managed by external staff. One has to note that the fibers and the mounts lose a few millimeters of length during development. Hence, it is important to consider this difference when cutting the fibers and not using the mounts more than two times. After the fibers had been polished, they were smeared with polishing paste, so one had to clean them again accurately. Furthermore, a few fibers had damages in their cladding after the cutting and polishing processes, so they had to be observed and sorted out exactly. The final fibers were covered with a layer of aluminum attached via sputtering by an external company. Because one end of the fiber must not be sputtered in order to be fixed on the SiPm, one had to prepare the

[1] Birgit Margit Lotz: Treatment procedure and light output analysis of scintillating fibers for scintillating fiber trackers [20]

fibers for the sputtering process. The open ends were covered with a Kapton-Tape. This tape was used since it is very heat-resistant and leaves only minimal residues, which is important because the tape has to be picked off again after the sputtering. In figure 4.1, the prepared and the final fibers can be seen. Once the fibers have their aluminum layer, one can establish if they were cleaned accurately enough. If residues were not removed, marks can be observed.

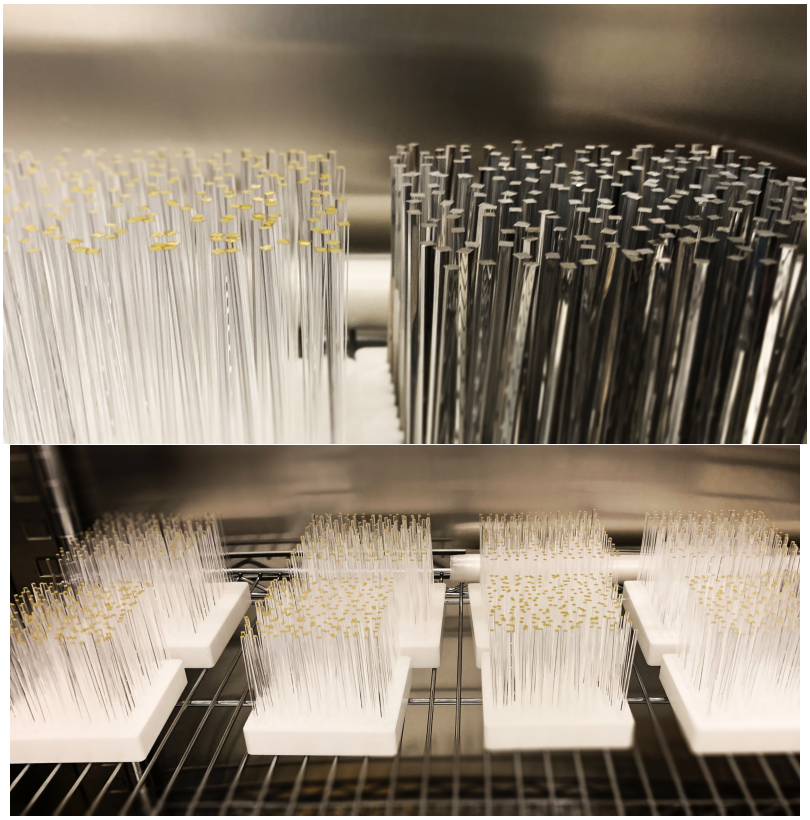

Figure 4.1: Covered fibers with and without aluminum layer

The finished fibers had to be placed in modules (Section 3.1.2). For this part, the critical point was not to damage the susceptible aluminum layer while putting the fibers at their tightly dimensioned places. Further, it was crucial to position the fibers in the correct arrangement because otherwise, no signal could be detected just like with a dead channel. To check the correct location of the fibers, a UV-light was used. Since the open fiber ends reflected the light brightly while the sputtered ends showed no effect, it could be verified simply if the fiber placement was correct. The final arrangement of fibers in their modules can be seen in figure 4.2.

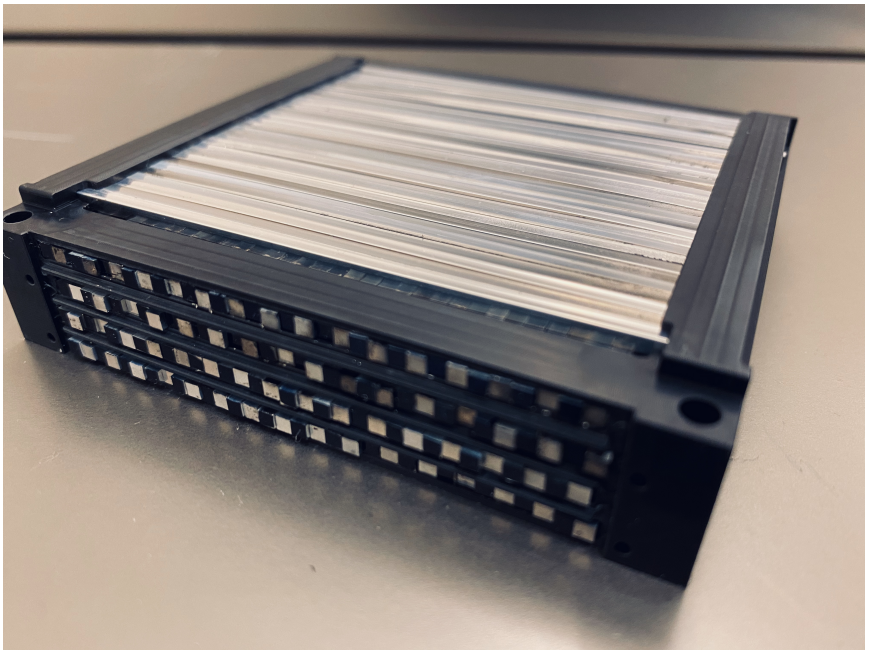

Figure 4.2: Completed module with finished fibers.

4.2 Design of a fiber sorting tool and a stand for the glueing process

In the last step, the fibers were glued to the SiPms. For this, the modules were placed on a mount that was accessible from all sides without touching other surfaces. This stand can be seen in figure 4.3. The fibers had to be pushed a few millimeters out of the module: the open ends at one, and the closed ends in the other direction. This process must happen from both sides simultaneously. Therefore, a fiber sorting tool was designed (figure 4.4). With the protruding polyvinylchloride sticks the fibers could be moved carefully without damaging their aluminum layer or cladding. The mount and sorting tool model was designed in SolidWorks [2].

[2] www.solidworks.com/de

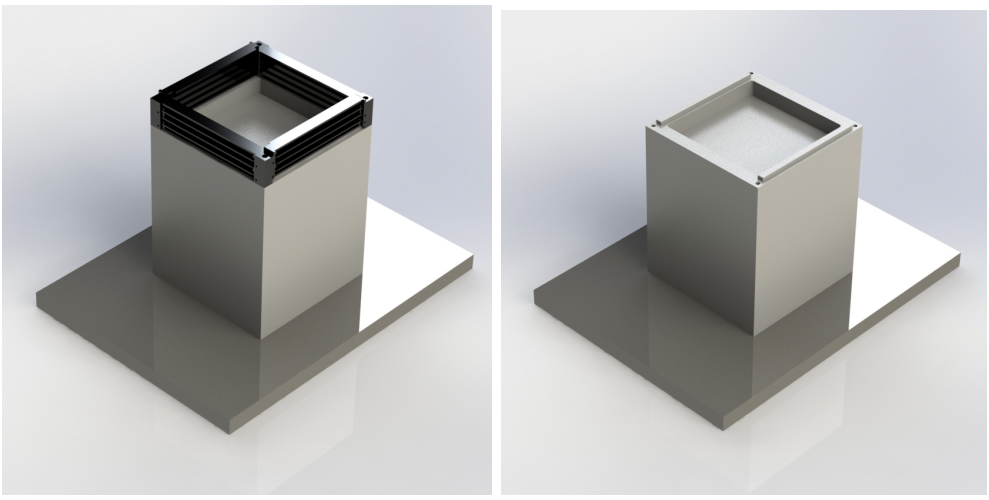

Figure 4.3: Mount for glueing process, with (left) and without (right) stack.

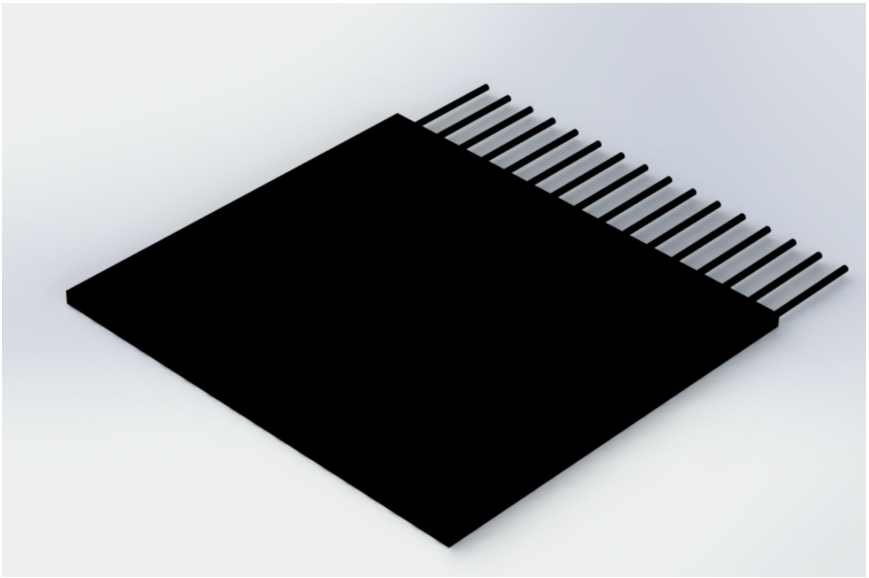

Figure 4.4: Sorting tool for the glueing process

Chapter 5

Classification

5.1 Fiber Analysis

For the quality control the variation within a single fiber and the variation of all fibers have to be qualified. This was achieved by measuring a quantity of fibers, which were placed under a radioactive strontium ${}^{90}_{38}\mathrm{Sr}$ source. Strontium decays via β^- decay:

$$ {}^{90}_{38}\mathrm{Sr} \underset{28.8y}{\longrightarrow} {}^{90}_{39}\mathrm{Y} + e^- + \overline{\nu_e} \underset{64.06h}{\longrightarrow} {}^{90}_{40}\mathrm{Z} + e^- + \overline{\nu_e} \tag{5.1} $$

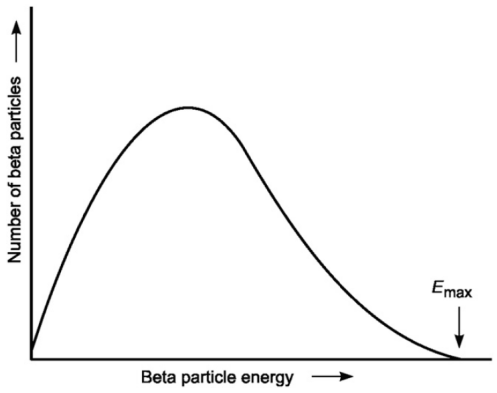

Figure 5.1: General beta-particle energy spectrum [21]

The spectrum of a β^- decay can be seen in figure 5.1. [21, p.49, p. 1319] Actually, the spectrum should have a second peak due to the second decay of ${}^{90}_{39}\mathrm{Y}$. In our setup, however, the source's scattering was very high. If the decay's electrons excite atoms

in the fibers – resulting in light emission – we expect that the second peak was not resolved. For our quality control, this does not matter. We are interested only in how far the measured peak positions shift. Ideally, the peaks of all fibers should be in the same position. Some sample plots of the measured fibersare shown in figure 5.2.

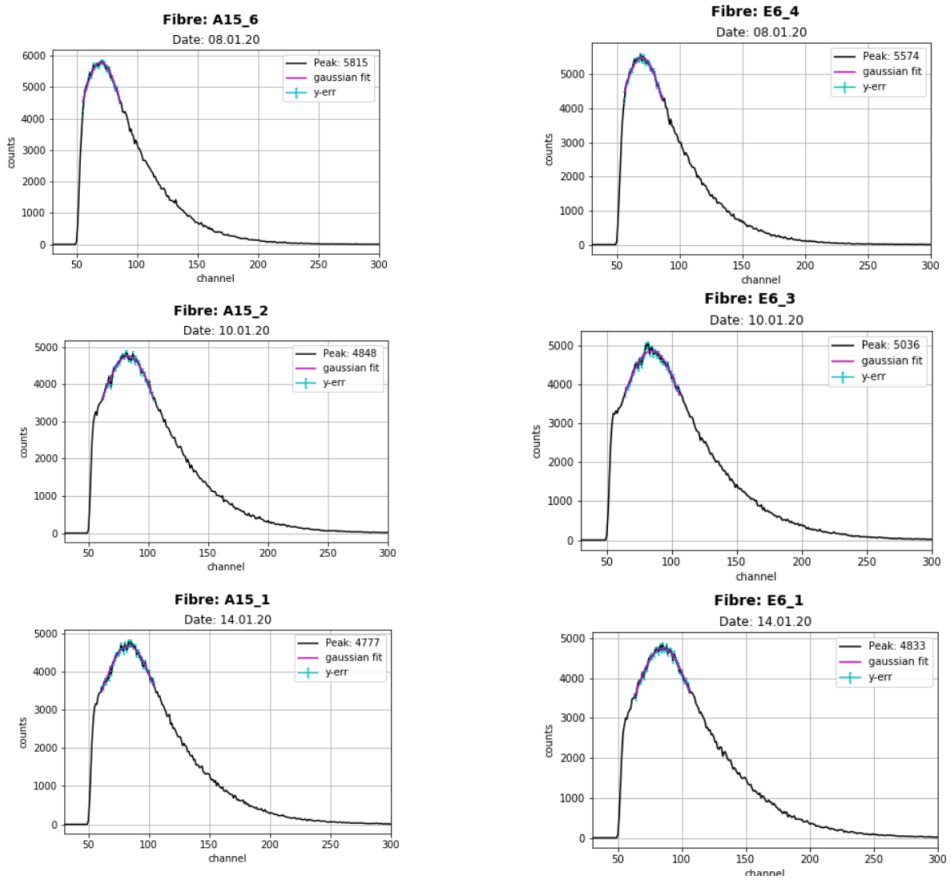

Figure 5.2: Sample plots of the beta-spectra of various single fibers. The peak position marked and fittet with a Gauss-Curve.

5.1.1 Variation of the single fibers

In order to quantify the quality of single fibers and the setup, some fibers were tested repeatedly. They were slightly moved and turned so that systematic uncertainties of the setup could be measured. With this information, an average mean peak position and every fiber's corresponding standard deviation could be determined. The result of some sample fibers can be seen in figure 5.3. The single fibers' resolution was calculated

with these values and finally resulted in an average standard deviation of ∼3% (figure 5.4). It should be noted that most of the fibers tested for this result were only measured on a single day. The result can, therefore, be considered a systematic uncertainty for that day. One obtains a far more realistic value by looking at the statistics of the fibers that were measured additionally on different days. With more than 20 measurement points, there are far more statistics available and additional uncertainties depending on the shape of the day are included. We used these fibers as reference fibers for further calculations. Two histograms of those measurements are shown in figure 5.3 (A15 and E6). For these fibers, a reference standard deviation of $\sigma_{sys} = 9\%$ was obtained for an average of the mean peak position of 76,5.

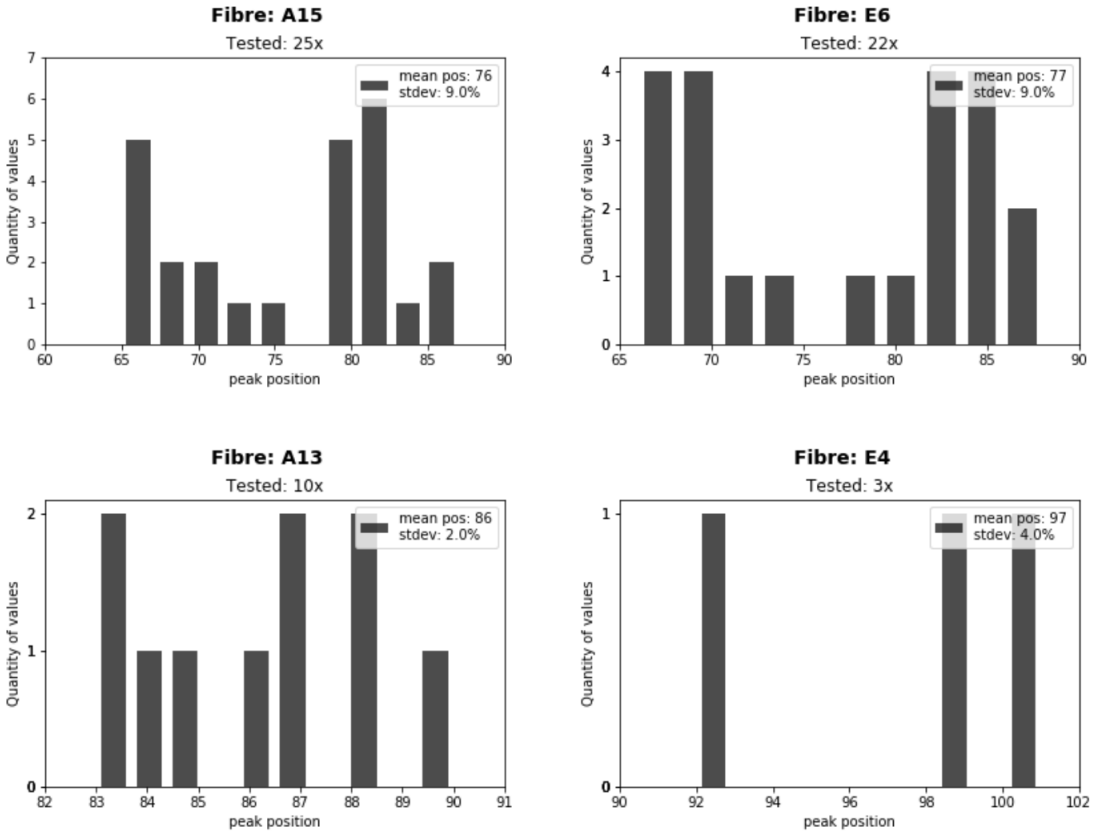

Figure 5.3: Sample plots of the variation of single fibers. Among others, fibers A15 and E6 were tested more often than other fibers and, as well, on different days, so they were used as reference fibers.

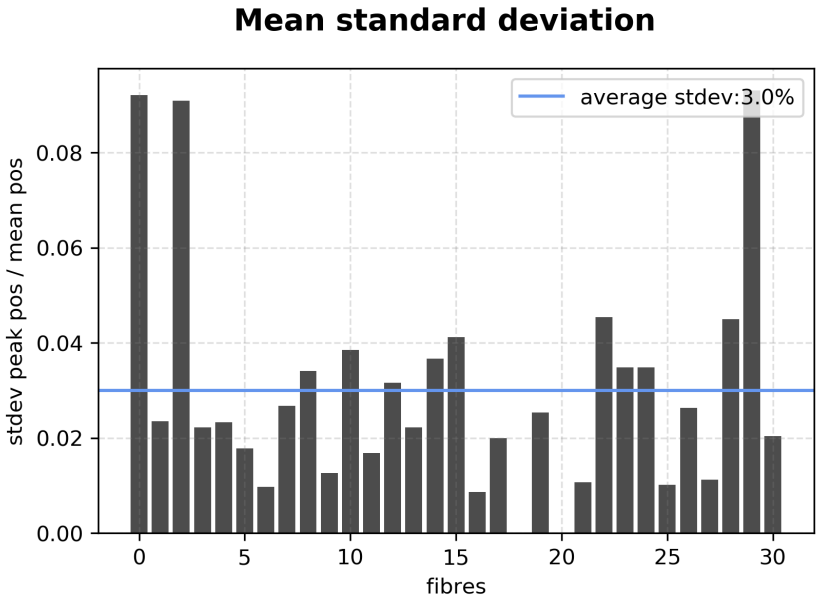

Figure 5.4: Absolute peak positions of all fibers.

5.1.2 Variation of all fibers

In the next step, this average of the mean peak positions of the single fibers were compared, so an average mean peak and the related position for all measured fibers could be calculated (figure 5.5).

For a qualitative context the absolute peak positions are important, which can be seen in figure 5.6 and 5.7. A benchmark for the expected peak position was defined with this information, and the related standard deviation was determined. This led to an overall uncertainty of σ_{tot}=13,1%. We expected a value for sigma lower than 10%. This result may be due to the circumstances that some fibers were not perfectly sputtered or still a little bit bent. The more often the fibers were measured, the more the aluminum layer came off and the source was not placed in the same position after each measurement.

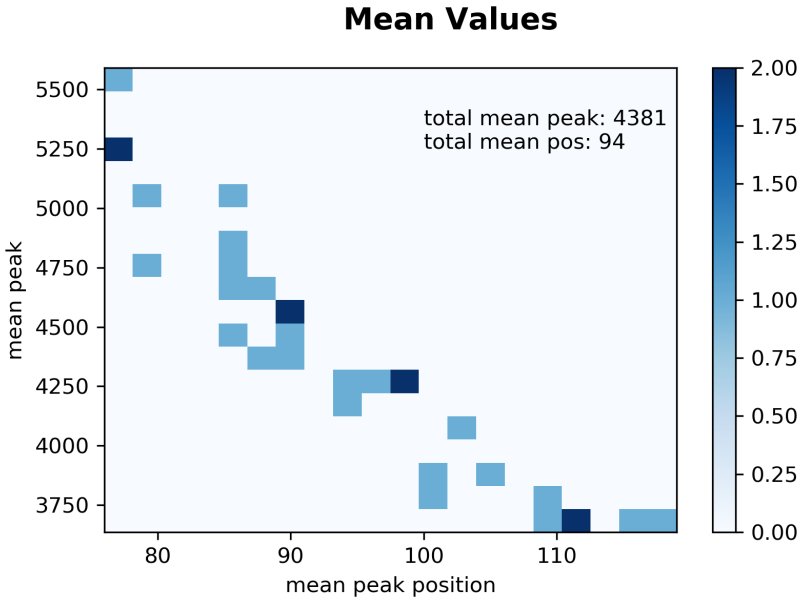

Figure 5.5: Average mean peak positions of all fibers.

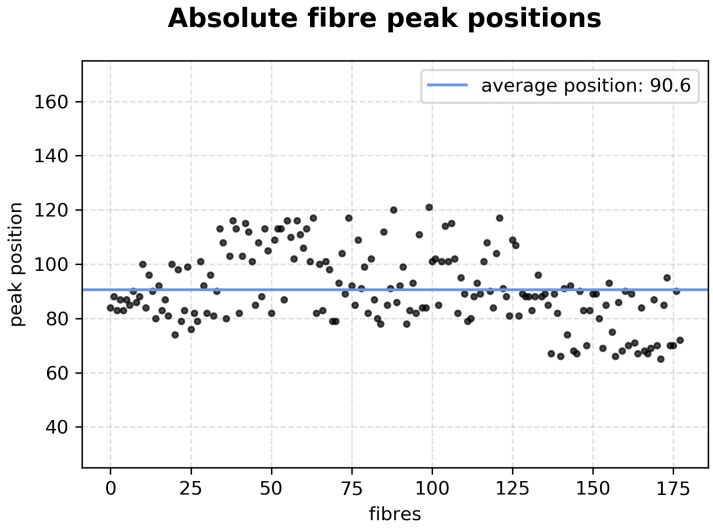

Figure 5.6: Absolute peak positions of all measurements

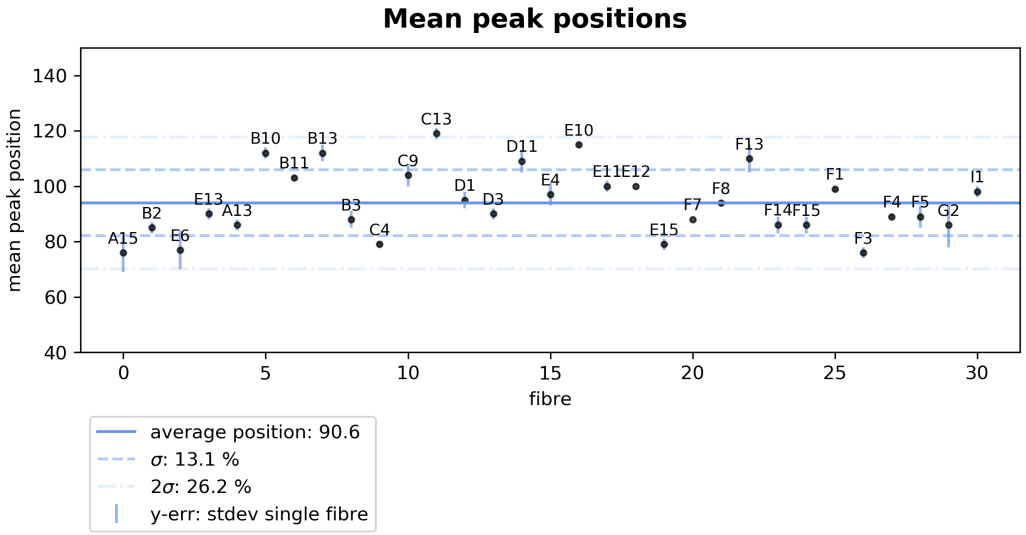

Figure 5.7: Absolute peak positions of all fibers.

5.1.3 Fiber Quality

To check the fiber quality, we are interested in the statistical uncertainty. This uncertainty we can determine with the following equation:

$$\sigma_{tot}^2 = \sigma_{stat}^2 - \sigma_{sys}^2 \Rightarrow \sigma_{stat} = \frac{1}{\mu_{stat}} \cdot \sqrt{(\sigma_{tot} \cdot \mu_{tot})^2 - (\sigma_{sys} \cdot \mu_{sys})^2} \tag{5.2}$$

$$\Rightarrow \sigma_{stat} = \frac{1}{90,6} \cdot \sqrt{(0,131 \cdot 90,6)^2 - (0,09 \cdot 90,6)^2} = 9,5\% \tag{5.3}$$

Here, μ is the absolute value taken from figure 5.7 and σ the percentage value of the standard deviation. The sigma values were determinded in section 5.1.1 and 5.1.2 and can be also seen in figure 5.3 and 5.7. So finally we reached a statistic error of 9,5% for the fiber quality. Thus we achieved a value that is satisfactory.

Chapter 6

Electronic Tests

6.1 Setup

For converting the light pulses into an electrical signal, SiPms from the Ketek company (section 2.3) were used which can be read out directly. The installed type is called PM3325-WB-D0 and consist of a 3x3 mm^2 Active Area with 25 µm Microcells, the applied voltage should be set on 29V. [22] The Ketek-Boards were connected to an Adapter-Board, on which there are four slots for Padiwa-Boards. A Padiwa-Board enables to set threshold settings and generates Time-over-Threshold (ToT) signals.[1]. The Padiwa-Boards were used in combination with a Triggered-Readout-Board (TRB). A TRB is a Time-to-Digital Converter (TDC) Platform, which is used for data processing and provides an interface. It involves also a Central Trigger System (CTS) which includes a web interface where all trigger settings can be handled. [24] Figure 6.1 and 6.3 show the components and the web interface of the CTS. For the light source, a LED flasher with two diodes of various light intensities is used. The schematic overview of the setup can be seen in figure 6.2.

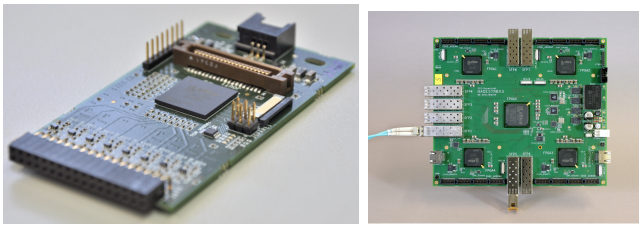

Figure 6.1: Left: Padiwa-Board. Right: TRB-System [24]

[1]With a ToT signal processing, the pulse width of the digital output is measured. For this, the voltage pulse is compared with a threshold voltage. [23]

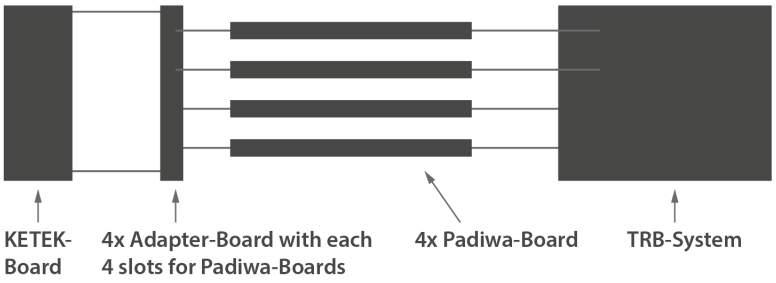

Figure 6.2: Schematic representation of the arrangement of the electronic components

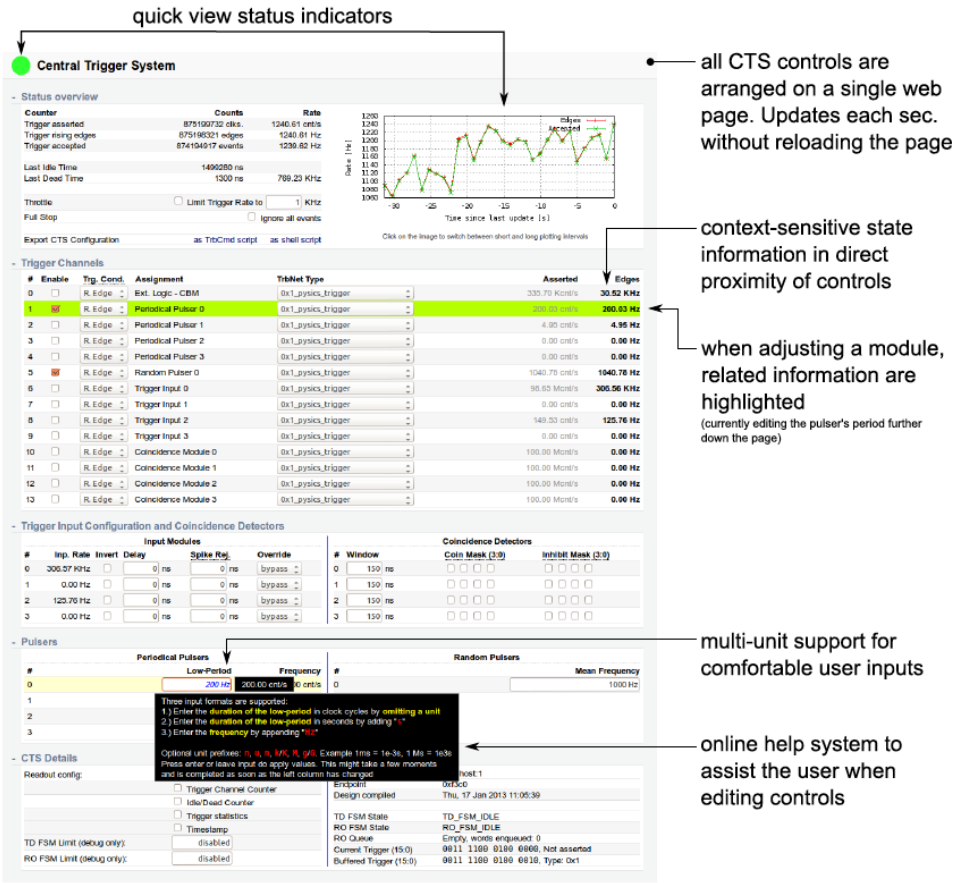

Figure 6.3: Web interface of the CTS. [24]

6.2 Measurements

6.2.1 SiPM Saturation Curve

As described in section 2.3, for each photon that is detected, one of the microcells of the SiPMs is "activated" and provides a given signal. The more cells have been hit, the lower is the probability that another photon will hit one of the "free" cells. Above a certain value, all cells are already triggered, so more light would not lead to any more signals. This is referred to as saturation. To characterize the Ketek-Boards, one has to quantify at which values the SiPMs saturate. For this, one KETEK-Board was irradiated with the LED-flasher. The referring signal amplitude was taken from an oscilloscope, so the SiPM-Output did not go to the Padiwas, but instead into the oscilloscope via a Lemo Adapter. This measurement was repeated with different offsets of the CTS. The associated saturation curves can be seen in figure 6.4. One can recognize that for higher signals the differences in the curves at various offsets become smaller. For an arbitrary unit of 200, the values are equal and the signal voltage no longer rises remarkably.

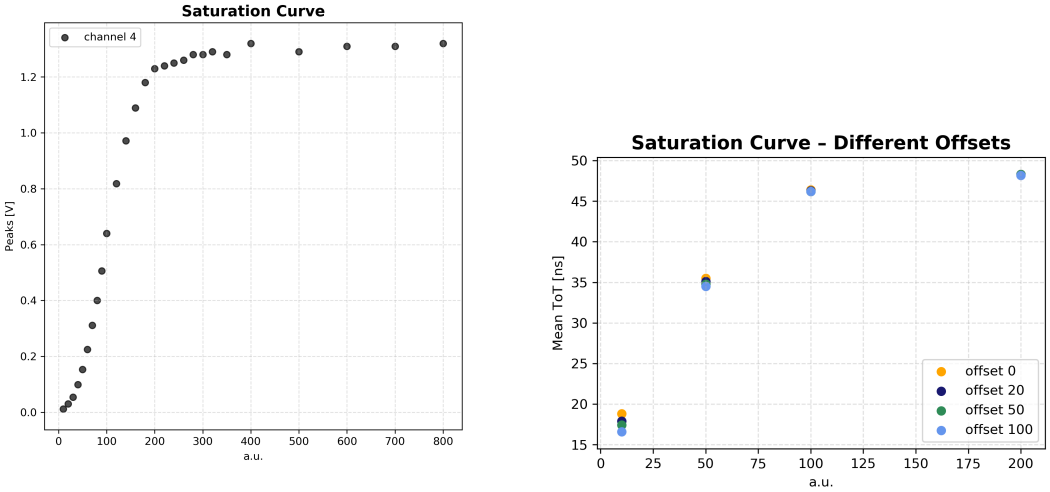

Figure 6.4: Saturation curve for characterizing the Ketek-Boards. The arbitrary unit refer to the intensity of the LED flasher.

6.2.2 Resolution

The steadiness of the SiPM-Output can be qualified with the same set-up as in section 6.2.1. The oscilloscope is able to return the mean value and the related sigma value to an output signal. The Ketek-Board was irradiated with the LED-flasher and the light intensity was varied. The higher the intensity the higher the signal which is equal to a higher mean value. The associated values to this measurement were taken after the oscilloscope has counted 2000 events. In figure 6.5 one can be see that the higher the signal the smaller is the fluctuation in comparison to the signal height. That means, that the resolution of the output-signal is getting better with increasing signals. The result was confirmed with a second measurement (6.6) in which the KETEK-Board was adapted to a Padiwa-Board. Again the light intensity was increased. The values of mean and sigma were determined with a gauss fit in root. This measurement establishes that the form of the resolution curve is equal. The width of the peak also behaves as expected and becomes narrower at higher signals.

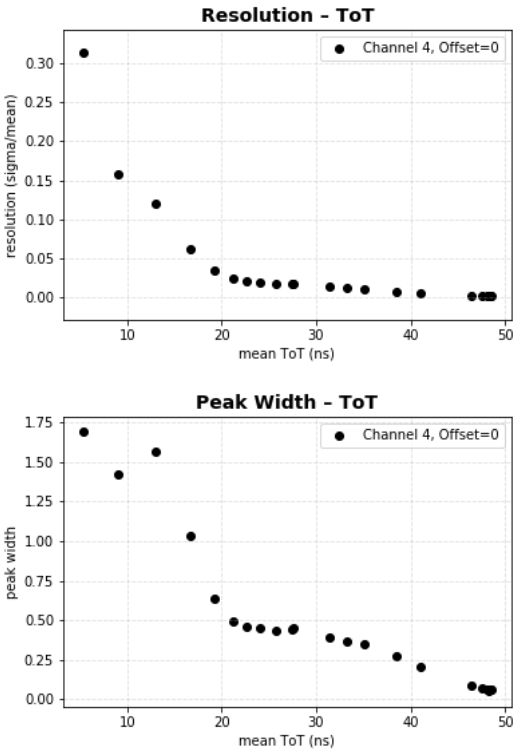

Figure 6.5: The resolution of the signal output, determinded with a gauss fit and ToT

.

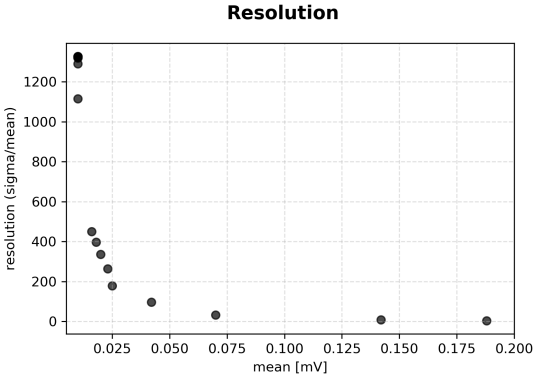

Figure 6.6: The resolution of the signal output, determinded with an oscilloscope

.

6.2.3 Caesium Source Measurements

For their final application, one has to qualify how the fibers react with radioactive sources. For this, a Caesium source was placed over a fiber and exactly one channel was irradiated with it. Figure 6.7 shows, that this channel led to a peak as expected. The adjacent channels indicated only some noise. This is a confirmation that no detectable crosstalk took place for these signal amplitudes. In section 7.2.4 further analyses to crosstalk will be described.

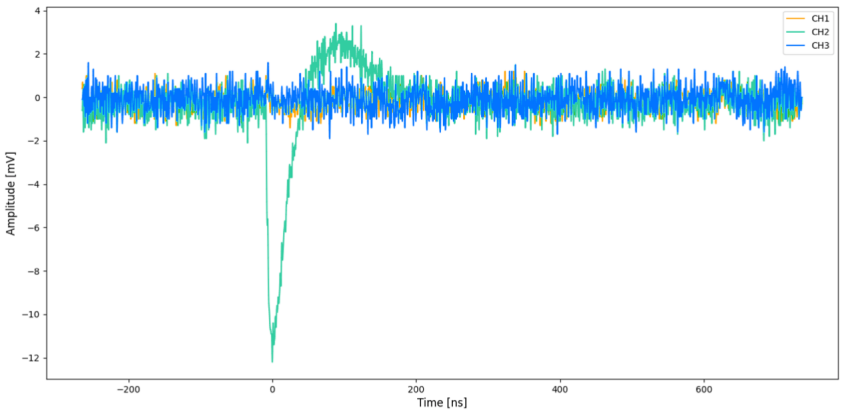

Figure 6.7: Spectrum of an irradiated channel with Caesium. Graphic: Stephan Königstorfer

.

6.2.4 Signal to Noise

In order to determine how signal and noise behave relative to each other with increasing offset, measurements with different light intensities and offset values were made. Figure 6.8 shows that with increasing offsets the ratio is also rising. Since the noise should get lower with higher offsets, this result is what we expected. With higher light intensity the curve is significantly steeper.

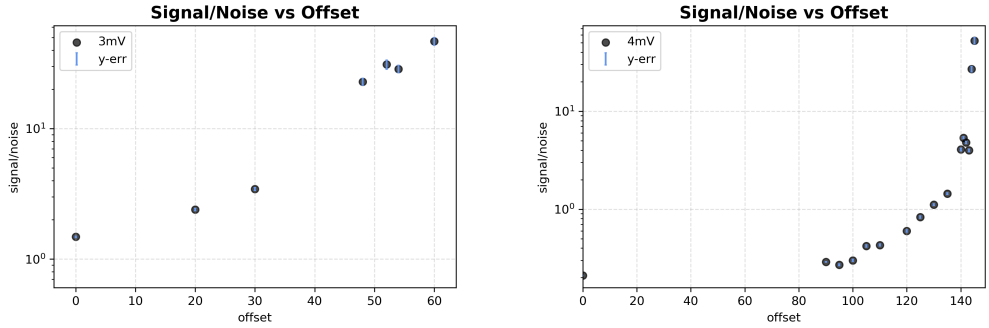

Figure 6.8: The behaviour of signal / noise at different light intensities.

6.2.5 Signal Rate to Offset

The observed signal rate in relation to an increasing offset provides some important informations. This measurement was made for an pulser rate of 100Hz and various light intensities, the corresponding curves can be seen in figure 6.9. The values above 100Hz can be dismissed as noise.

Above a certain value for the offset, the observed signals were no longer conform with the input rate disappear. Thereby, it is known how high the offset can be set to still see signals. Furthermore, a kind of transformation factor from light intensity to offset can be concluded. For example, for a light intensity of 200 in arbitrary units, in this case an operating voltage of 55mV of the pulser, the signal rate disappears for an offset of about 5000, so an ats4-value of 200 can approximately be translated to an offset of 5000.

Further, we can read out the width of the peak. If we stay with this example, it can be observed that for an offset of ∼4900 there is still a signal of 100Hz, for an offset of ∼5400 nearly none. This offset difference of 500 describes the peak width. Before it was determined that an offset of 5000 is ∼ 55mV, so an offset of 500 leads to ∼5.5mV. It has to be noticed that this is a very rough approximation because the signal is not linear and the just assumed 1:1 translation is in fact not correct, but it delivers an

estimate within an order of magnitude. One can see that the larger the offset values the lower the linearity.

Finally, the curves demonstrate that measurements with a light intensity below ~2.5mV are not possible with the used set-up because the input rate of 100Hz cannot be achieved.

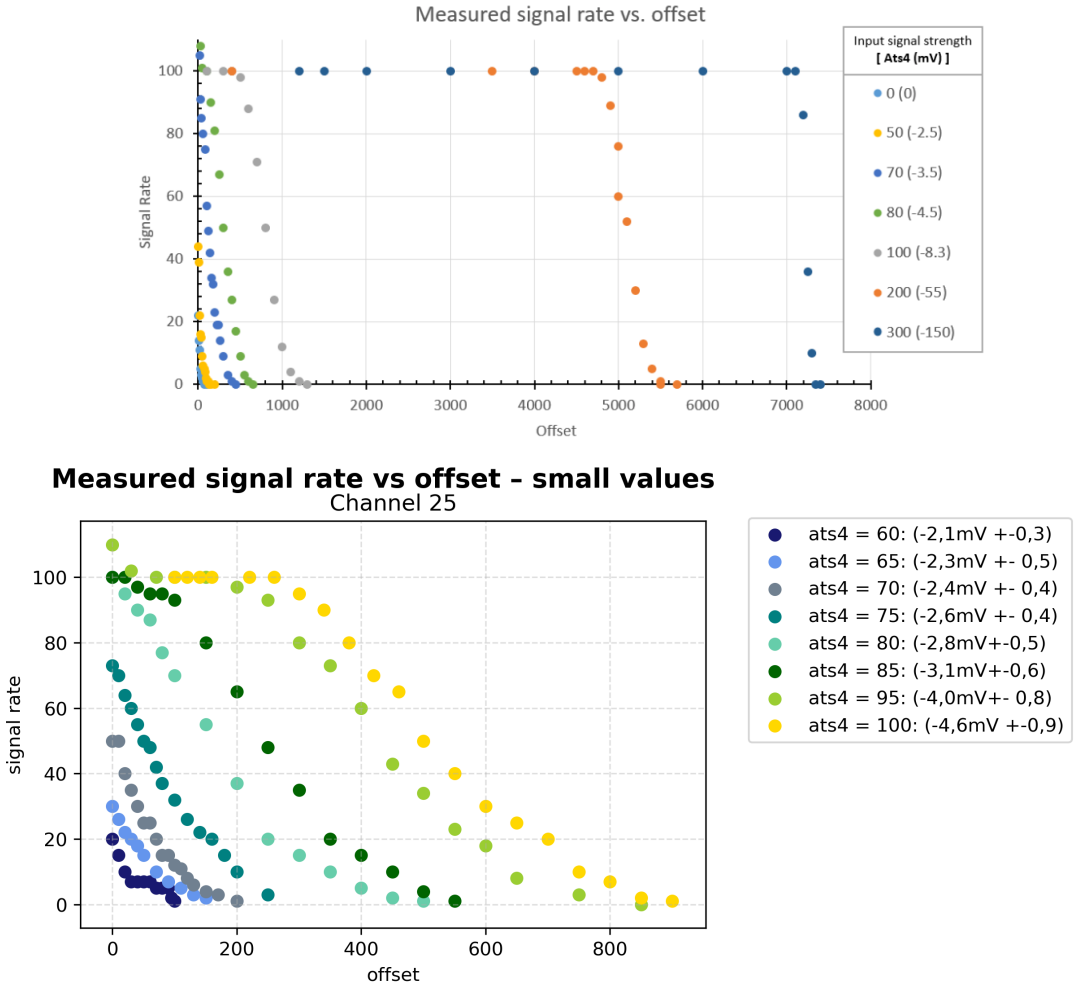

Figure 6.9: Signal rates to offset. Ats4-Values are arbitrary units and depend on the light intensity of the pulser. It has to be considered that in both measurements the same ats4-values result in different voltages. This is because the measurement for small values were performed with a covered pulser. Top graph for high offset values adopted from Berkin Ulukutlu.

6.2.6 Systematic Tests of the Ketek-Boards

Finally, all boards were tested for their functionality. These tests had to be done in a cleanroom. Four Padiwas were available for this measurement, so 128 channels were inspected at the same time. All boards were successively irradiated with the LED flasher. With the analysis feature of the TRB-System anomalies on the boards, for example, dead channels or significant noise were observed and subsequently noted. In figure 6.10 two sample plots of different Ketek-Boards can be seen. One shows a board without any unwanted features, the other one represents an example of a dead channel. Nearly all boards have been flawless.

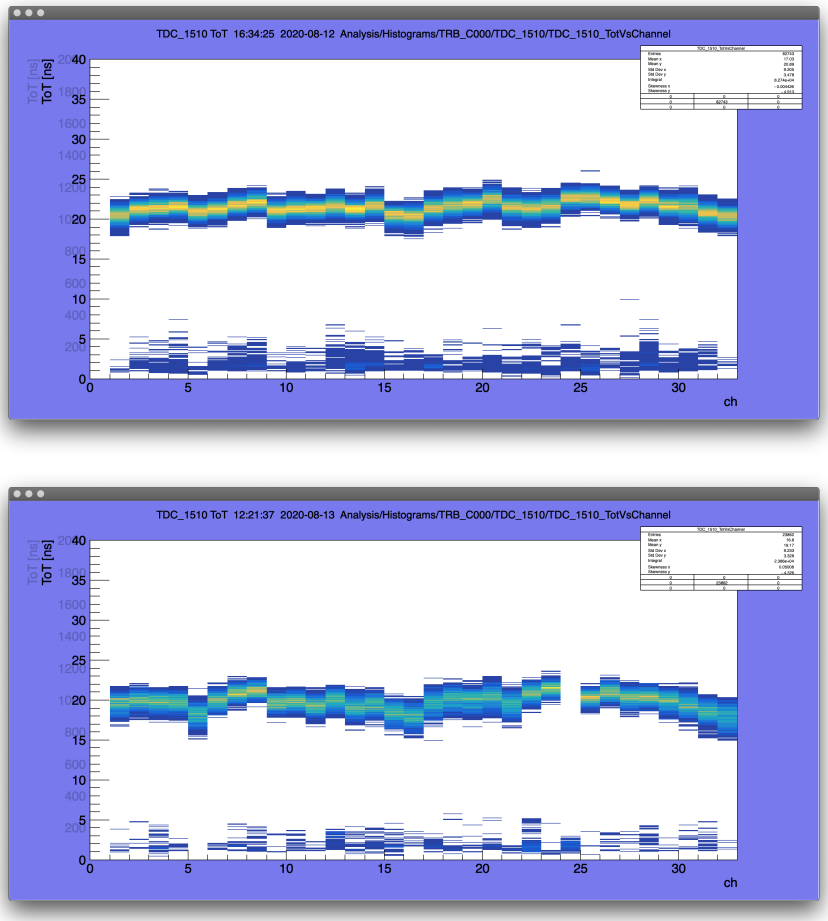

Figure 6.10: Sample plots of the systematic board tests. At the bottom one can see that channel 24 is dead.

Chapter 7

Beam Test

For testing as well as calibration purposes and to qualify the functionality of our electronic setup's readout, the ADU of the detector was performed at a pion and proton beamline at the Paul-Scherrer-Institute (PSI). The calibration of all produced modules will not be part of this thesis; instead, it is focused on different tests with one testing-module. This module was irradiated in three different angle positions with various overvoltages and threshold settings. The direction of the beam and fibers can be seen in figure 7.1.

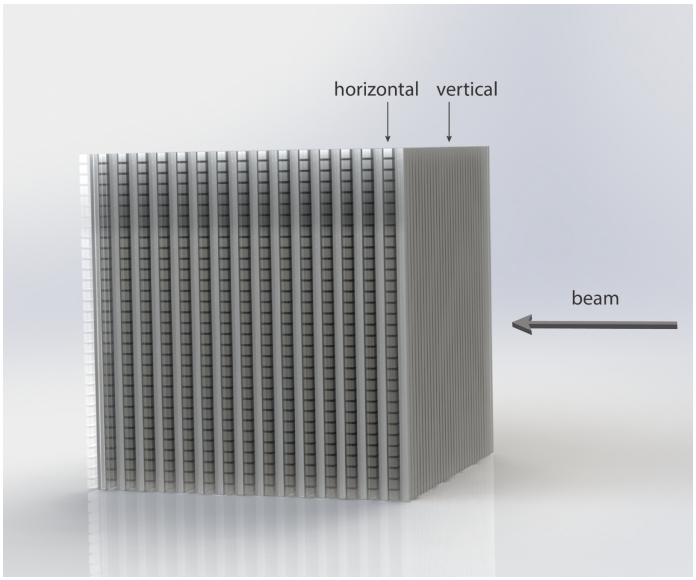

Figure 7.1: Schematic overview of the beam- and fiber-directions. Graphic created with SolidWorks.

7.1 Single Channels

Looking at the single channels' 1D histograms (figure 7.2), we find that the pions have an almost ideal Gaussian curve. For the protons, on the other hand, the Gaussian curve is less pronounced. Besides, there is much noise in these measurements.

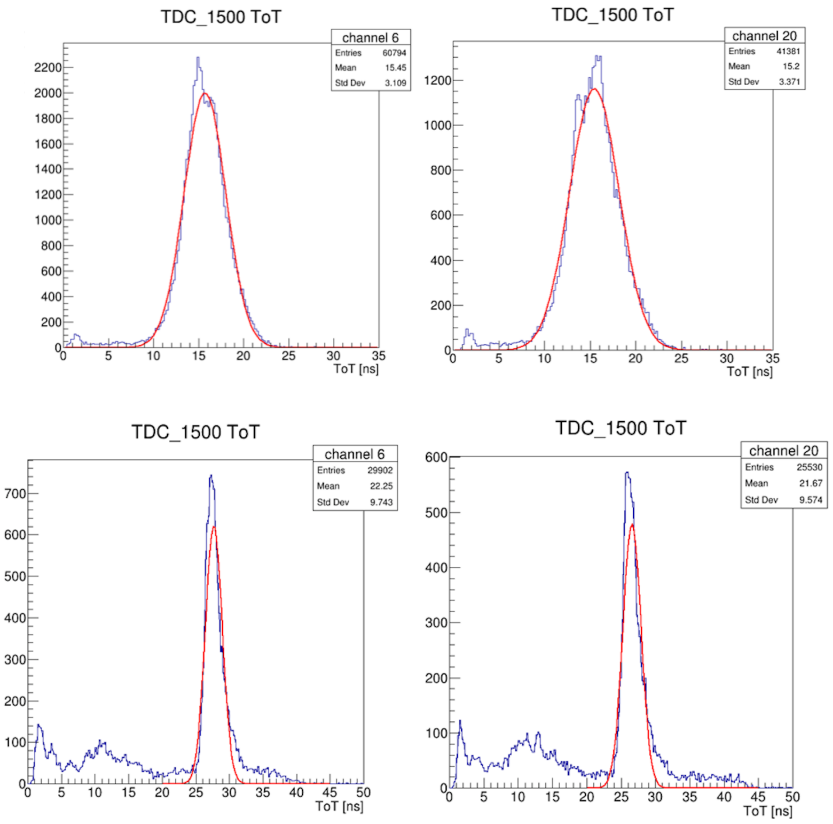

Figure 7.2: Sample plots of some 1D histograms. 29V.Trigger Rate 50kHz. Treshold 100. Top: Pion-Beam. Bottom: Proton-Beam

7.2 ToT Histograms with different configurations

7.2.1 Preparation

For a general overview, all layers of the test module were irradiated with pions and protons. In figure 7.4 the 2D histograms of a pion run can be seen. One can find that in addition to the peak at ∼15ns, remarkable signals are also visible in the range around 80ns. A more detailed analysis had shown that this additional signal occurred when two hits were detected in one event. A sketch of this process can be seen in figure 7.3. For all further analyses the data, where only the first detected hits were included, will be used.

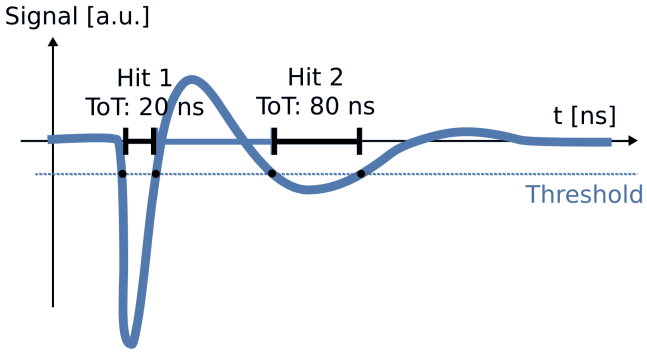

Figure 7.3: Draft of the Signal with more than one hit in event. Graphic: Berkin Ulukutlu.

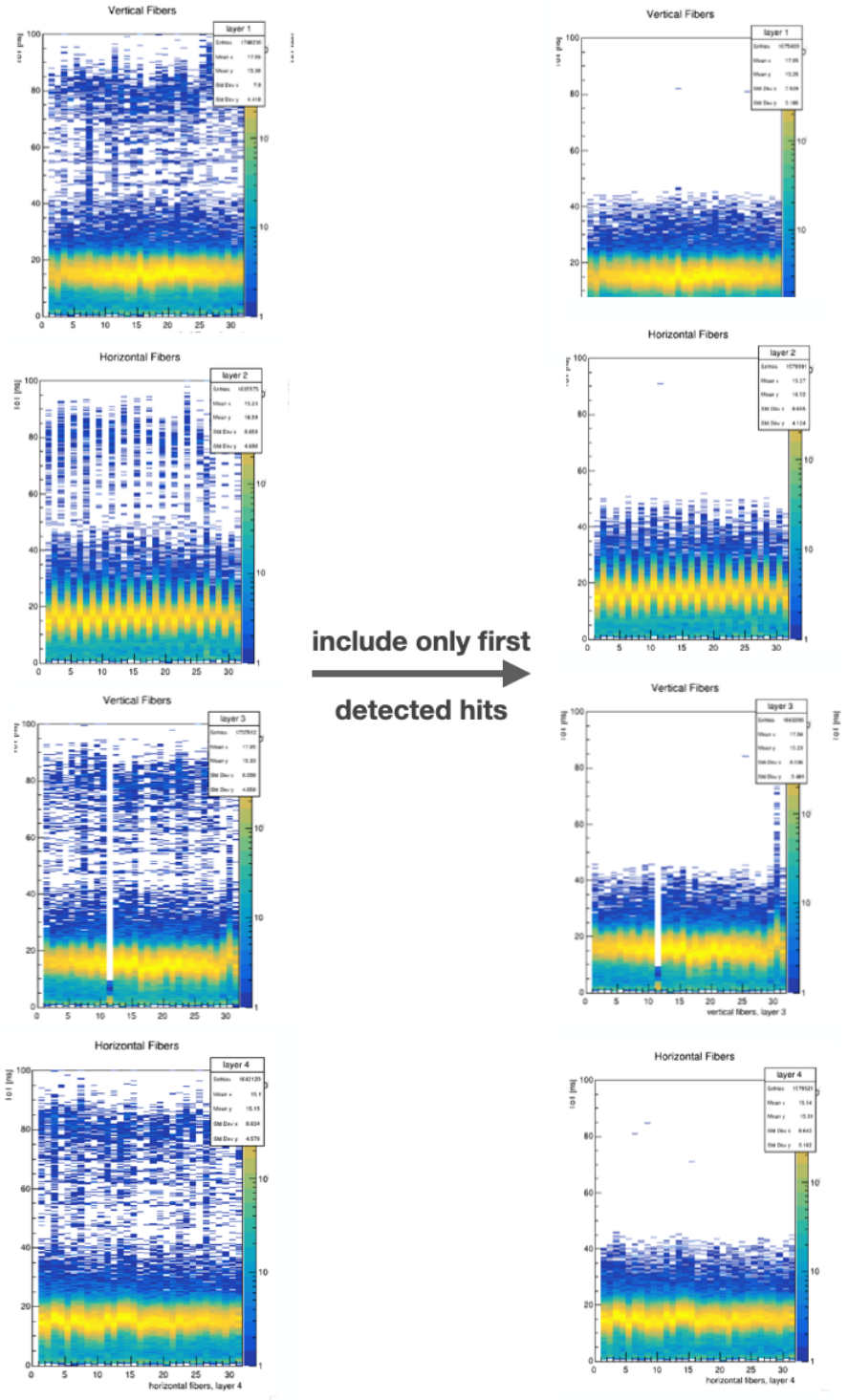

Figure 7.4: 2D-Histograms with Pion-Beam. Layer 1-4. Overvoltage 29V. Treshold 100. Trigger Rate 50kHz. angle 0°. Left: All detected hits are included. Right: Only the first detected hits are included.

Since the Padiwas have different gains, some of the fibers have a higher ToT-Signal than others. These differences can be seen especially well in figure 7.4, horizontal fibers, layer 2. In order to compensate for this difference, all fibers have to be calibrated to level the ToT-Signal for every measurement. For this calibration, the determined mean values of the Gauss-Fit of the pions' and protons' 1D histograms (section 7.1) are used. The mean values give the corresponding ToT values. For every fiber, this ToT value of proton and pion is plotted against reference ToT values (figure 7.5). For pions, the reference value is chosen as 15ns, for protons 26ns. A straight line is fitted to the two resulting points and leads to values for the slope and the y-axis intercept. The slope provides the multiplicative calibration parameter. The y-axis intercept leads to an additive factor, which compensates the offset. With this parameter, the measured ToT signals are adjusted. This process has to be done for all TDC's. Finally, this calibration can be used for all measurements, for proton and pion runs, also for different energies and independent of threshold and angle settings. The calibrated histogram of the pion run can be seen in figure 7.6. For further analyses, the calibrated data will be used.

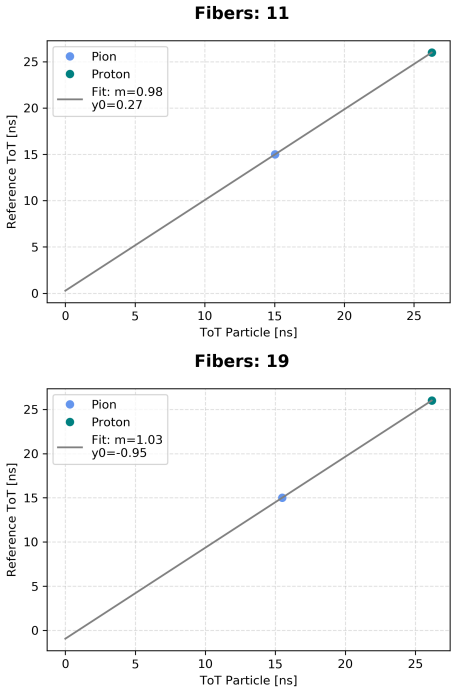

Figure 7.5: Sample plots of the calibration fit. For the y-axis, reference ToT values are used (pions: 15ns, protons: 26ns). The fit parameters lead to the required calibration parameters.

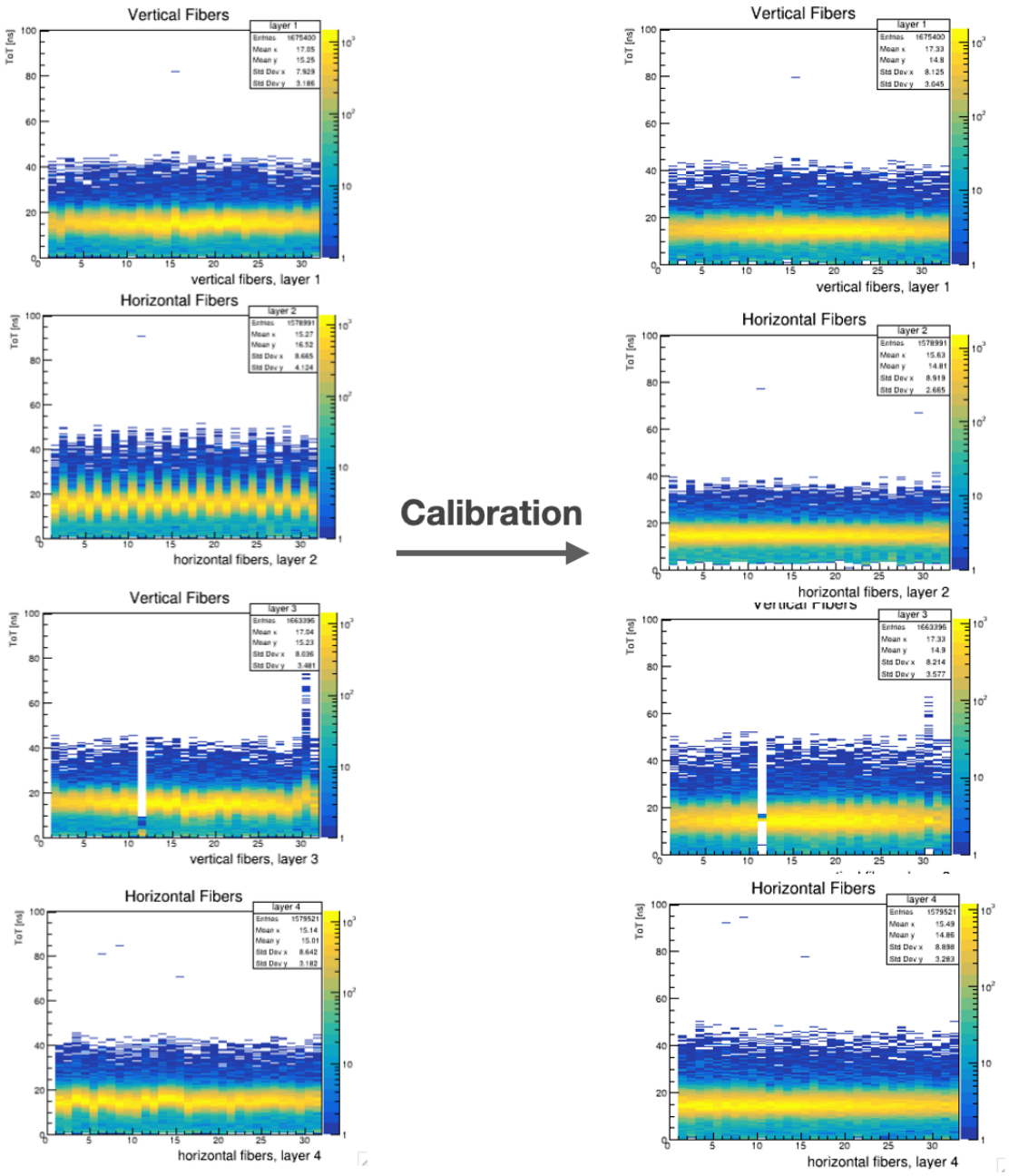

Figure 7.6: Calibrated pion run with the paramters determinded in section 7.2.1.

7.2.2 Interpretation

The arriving pion beam had a momentum of 450MeV/c. The different materials, the particle had to pass, and the referring energy loss can be seen in the appendix, figure 10.1 and 10.2. It can also be read from this that the particle had a total energy loss of ∼31MeV. These calculations, as well as the following calculations about the energy losses for protons, were done with WebAtima[1]. With this energy loss, which is smaller than the total energy of the pions, the particles should pass all layers. This theoretical result can be approved with the left histogram in figure 7.7, where one can see that in all layers, a clear signal at ∼15ns exists. Furthermore, from figure 10.2, it can be seen that in all layers, the energy loss of the pions is nearly constant and the specific energy loss is near the minimal energy loss. From this, one can conclude that we see MIPS (section 2.4). The measurement was repeated for 45°and 90°(figure 7.7). It can be confirmed that for 90°, as expected, the vertical fibers experience insignificant changes because this rotation did not change their geometrical area for light input. In contrast, the signal distribution of the horizontal fibers is significantly flatter. This difference can also be observed in all layers for an angle of 45°.

For the proton run (figure 7.8) – as expected – the measurement leads to significantly higher signals since a pion with ∼135 MeV has a remarkably smaller rest energy than a proton with ∼ 938MeV [26]. The rest energy is the mass, which results in a much larger beta for pions than for protons at the same momentum. From the Bethe-Bloch formula (section 2.2) it can be shown that this leads to a higher energy loss at the same momentum. The dead channel, which was already identified in section 6.2.6, can also be observed in these histograms.

The measurements were done with different settings for the proton momentum. First, the arriving proton beam had a momentum of 310MeV/c. In figure 10.3 and 10.4 in the appendix, a total energy loss of ∼49,8MeV/u and the corresponding materials can be seen. Since the there is no energy conversion taking place in layer three, we assume most of them stopped in layer two. This can be confirmed with the top histogram in figure 7.8 in which one can see that the clear signal at ∼26ns disappeared. Instead, the pions' signals can be observed again at ∼15ns since the pions have a lower energy loss than the protons. Subsequently, a proton momentum of 322MeV/c was configured. The material, which the protons had to pass, did not change. The referring energy loss of ∼ 53,7MeV/u (figure 10.5) suggests that not all protons passed through all layers. In the bottom histogram of figure 7.8, however, one can see that this is the case. It is possible that the material specifications were not precise enough to support the experimental result.

[1] https://www.isotopea.com/webatima/

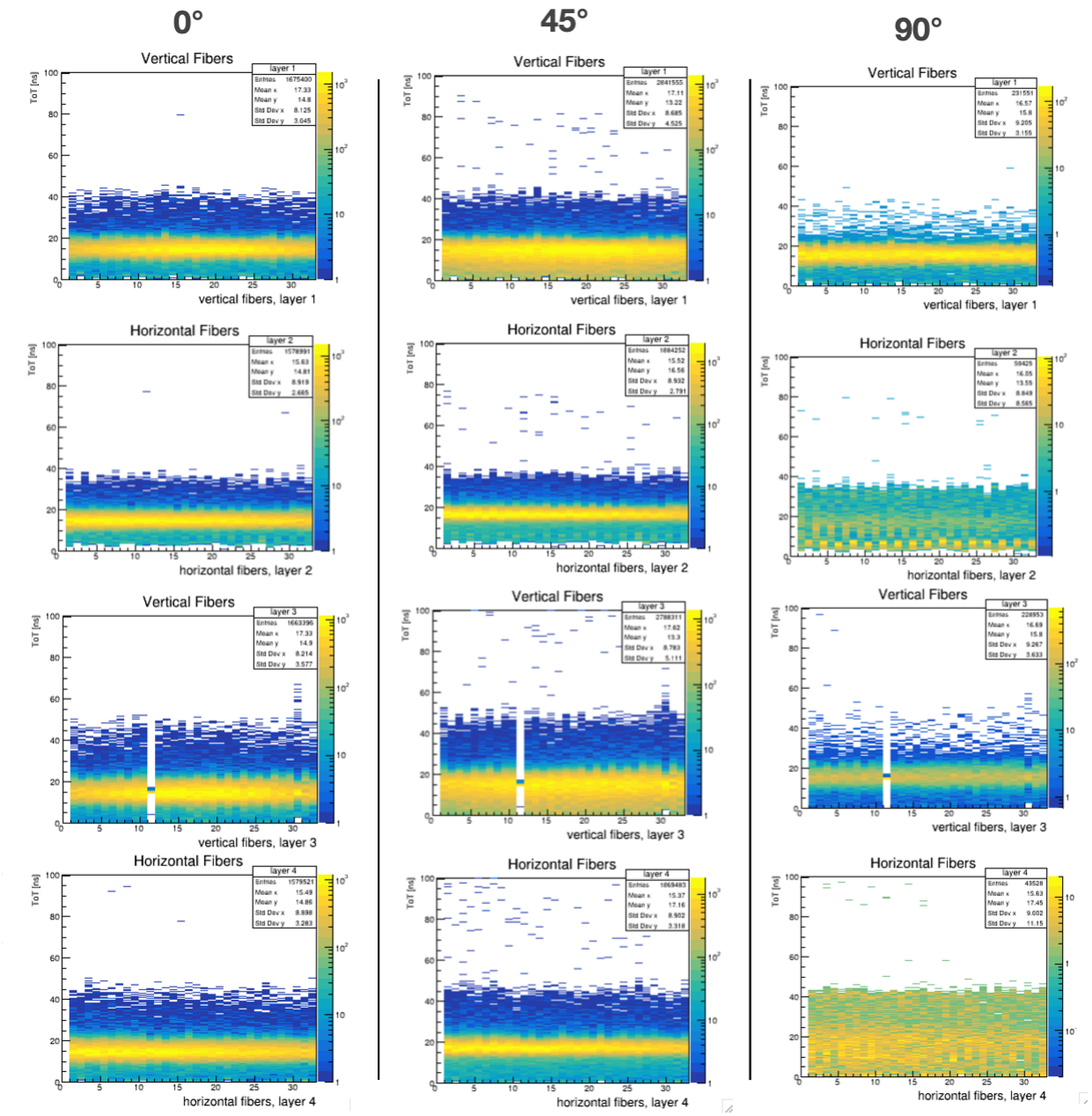

Figure 7.7: Calibrated pion run, only first hits in event Layer 1-4. Overvoltage 29V. Treshold 100. Trigger Rate 50kHz. Top: angle 0°. Middle: angle 45°. Bottom: angle 90°.

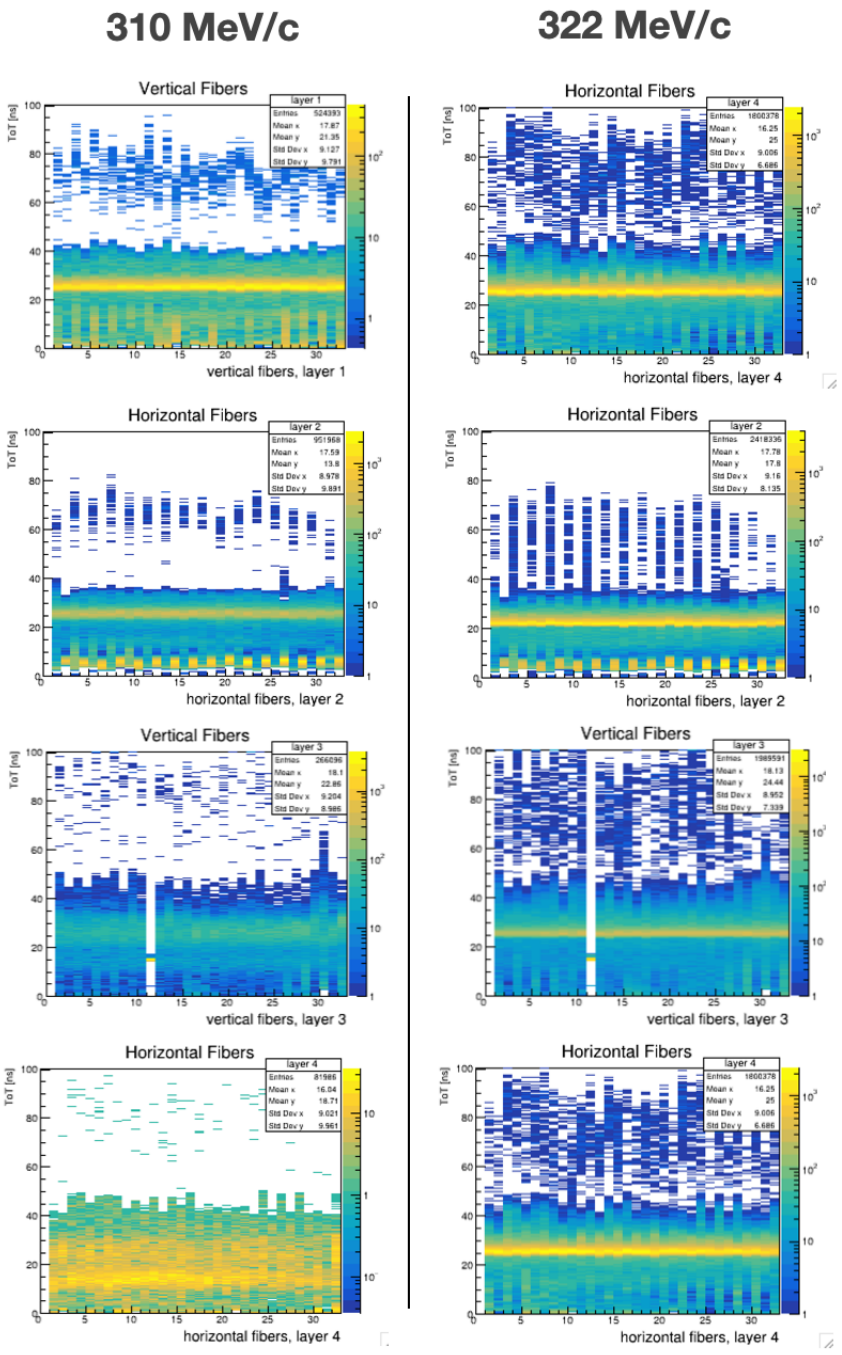

Figure 7.8: Calibrated proton run. Layer 1-4. Overvoltage 29V. Treshold 100. Trigger Rate 50kHz. angle 0°. Left: Protons with p=310MeV/c stopped in layer 2. The different scale in layer 3-4 has to be noticed. Right: Higher beam rate; Protons with p=322MeV/c penetrated all 4 layers.

7.2.3 Signal to Voltage

In order to understand how the signals behave due to the voltage, the voltage was increased step by step while the other settings remained the same. Figure 7.9 confirmes that – as expected – the signals rise linearly with the voltage.

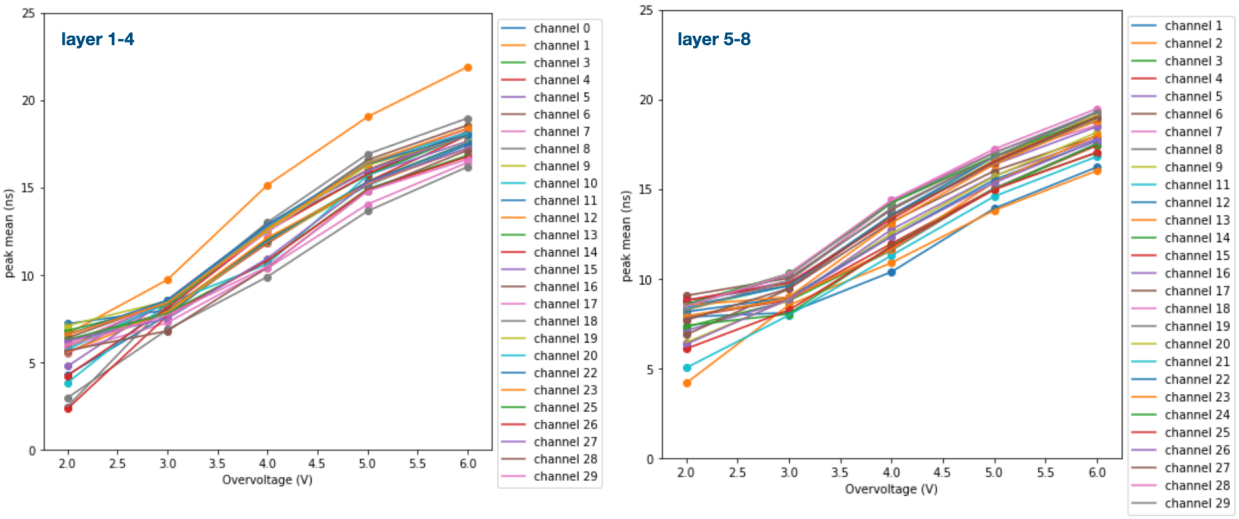

Figure 7.9: Layer 1-8. 26-30V.Trigger Rate 50kHz. Treshold 100.

7.2.4 Crosstalk

Since the hits are sorted on each layer for every event, the hit with maximum ToT is extracted, and a time window of 20ns is applied around it. Thereby, one can determine whether crosstalk takes place (figure 7.10). The time window is set to ensure that only actual signals are included (compared figure 7.3). The fiber which was hit, is centered in the plot. The neighboring fibers do not show relevant signals. From this, one can conclude that for pions, no remarkable crosstalk can be seen. However, with protons the neighboring fibers show significant signals leading to the conclusion that crosstalk is noticeable. Due to the higher energy of the protons, this behaviour is plausible.

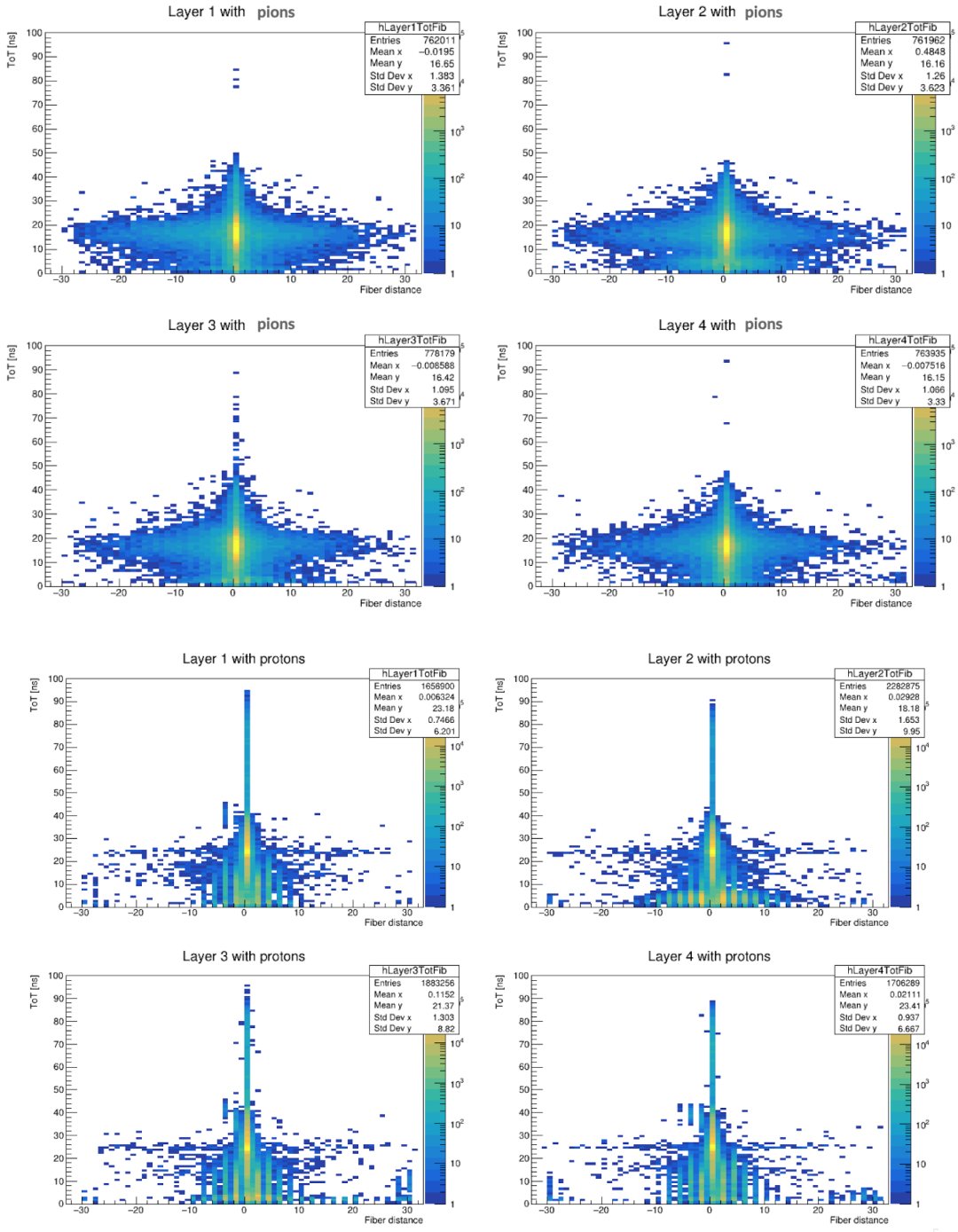

Figure 7.10: ToT of hits vs the order of neighborness to the fiber with the initial hit. Top: Pions. Bottom: Protons with higher beam rate so particles do not stop in the second layer. For protons more crosstalk than for pions can be observed. Graphic: Berkin Ulukutlu

7.2.5 Tracking

The concepts and calibrations that have been done in this thesis are the basis for a further analysis, that will be able to fully track the particle three-dimensionally. For the sake of completeness the concept and challenges of tracking with this detector is briefly discussed.

By tracing the path a particle has taken, further conclusions could be drawn about possible pile-up or the particle's trajectory. In figure 7.11 an event with two particle impacts can be seen. In layers one and three, one particle hit fiber 12, and a second particle hit fiber 18, respectively. In layer two, these two hits can also be seen at fiber 2 and 12. If this particle trajectory was perfectly perpendicular, we would expect that the same fibers showed a signal in layer four. Since this is not the case, one can conclude that the particles came with an angle and hit a different fiber or went out of the module area. Another possibility can be that the particle encountered something else before it reached the module.

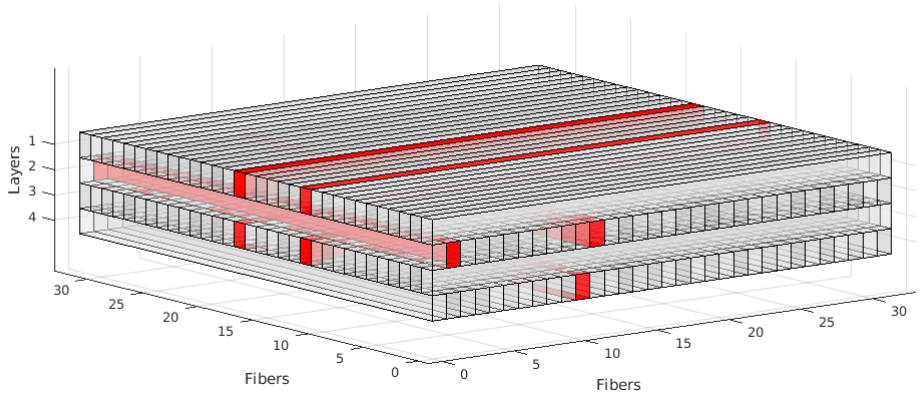

Figure 7.11: Tracking of a double hit event. Pions, 0°. Graphic: Berkin Ulukutlu

In figure 7.12 another event is shown. Again two particle hits can be observed (layers 1 and 2, again slightly shifted). However, we can also recognize the neighboring signals in layers 2 and 4, where two fibers side by side detected a hit. Since the probability that a particle hits two neighboring fibers is minimal, one can conclude that so called pile up took place: One particle was accidentally observed as two hits.

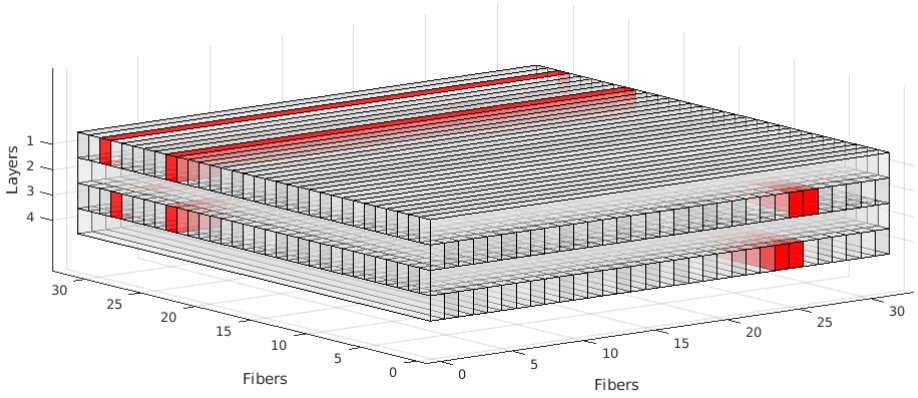

Figure 7.12: Double Hit event with pile up. Pions, 0°. Graphic: Berkin Ulukutlu

Chapter 8

Summary and Outlook

In the course of this work, the challenges of detector construction, a compliant electronic readout, and a final check at a particle accelerator at the PSI were presented. A central part of the detector construction was the production and quality control of scintillating plastic fibers. For the latter, the fibers were irradiated with $^{90}_{38}$Sr, resulting in a β-spectrum. The measured spectra of various fibers were compared, which leads to a standard deviation of σ_{total}=13,1% and $\sigma_{systematic}$=9,0%. With these values, one can determine a statistic error of $\sigma_{statistic}$=9,5%, yielding a value for the fiber classification.

For implementing the electronic readout system, a setup with SiPm-Boards, Adapter-Boards, Padiwa-Boards, and a TRB-System, which includes a central trigger system, were installed. For the readout, the ToT method was used. Various tests confirmed that the signal curve saturates at specific light intensities and that the resolution of the output-signal is getting better with increasing signals. With a Caesium source, we investigated, if crosstalk takes place. For the measured signal amplitudes, no crosstalk can be observed. To determined the ratio of signal and noise, measurements with different light intensities and offset values were made, leading to the result that the ratio is also rising with increasing offsets. Further measurements with various offset provide knowledge about the maximum offset set before the signal rates can no longer be observed. From these measurements, we can also conclude that the larger the offset values, the lower the signal's linearity. Finally, a systematic test of all SiPm-Boars was made. It can be established that nearly all boards are flawless.

Most recently, a beam test with pions and protons at the Paul-Scherrer-Institue was performed. With a voltage of 29V for pion runs, a ToT signal of $\sim$15ns, for proton runs $\sim$26ns, was determined. One can confirm that as expected the signals rise linearly with the voltage. Furthermore, by tracing the trajectory a particle has taken, we established that sometimes it comes to pile up events.

To classify this pile up more precisely should be part of further analyses. It also

remains an open question whether crosstalk occurred during the measurements and whether electronic or optical effects were involved. In order to be able to use the measured values of the radiation test qualitatively, the detector modules have to be calibrated to obtain comparative values.

Overall, the project's goal was achieved: We were able to confirm that both the chosen detector design and the electronic readout can be used to measure pions and protons and provide meaningful measurement results.

Chapter 9

Acknowledgements

First of all, my thanks go to the inspiring Prof. Laura Fabbietti, who took me by the hand, believed in me and entrusted me with this highly exciting and instructive project. My thanks also go to Stephan Königstorfer, who never got tired (or at least pretended to) to explain things to me ten times, if necessary, until I finally understood them (or at least pretended to). A special thanks goes to Thomas Klemenz, who was reliable and more than helpful at any time of day or night, on weekends and during his vacations, and who often saved me from complete despair. And my last, but very special thanks go to Markus, who reminds me every day that studying physics was the best decision of my life, even if I constantly claim otherwise.

Chapter 10

Appendix

10.1 Values for Material and Energy Loss

10.1.1 Pions

Matter

#	name	matter	density (g/cm^3)	thick. (mg/cm^2)	thick. (cm)
0	Air	Air	0.001205	361.5	300
1	E18 plastic set up	BC_400	1.032	1.65e+3	1.6
2	E18 trigger plate	BC_400	1.032	722.4	0.7
3	Plastic Fiber Layer 1	BC_400	1.032	206.4	0.2
4	Dark Box	Al2O3	3.97	397	0.1
5	Plastic Fiber Layer 2	BC_400	1.032	206.4	0.2
6	Sputtering	Al2O3	3.97	1.99	5.0000e-4
7	Plastic Fiber Layer 3	BC_400	1.032	206.4	0.2
8	Plastic Fiber Layer 4	BC_400	1.032	206.4	0.2

Figure 10.1: Values for the material, the pions had to pass. The sputtering has no relevant part, therefore it appears in the list only in one place to illustrate the minor role. [25]

Total Results

Projectile: 1H @ 101.5916MeV/u Change

E_{out} = 70.7406 MeV/u E_{loss} = 31.0755 MeV σ_p/p = 4.532e-3 Reaction rate: 0.012

Bρ = 1.24268 Tm σ_E = 0.6186 MeV/u σ_a = 26.1281 mrad

β = 0.369031 TOF = 23.519240 ns σ_{pos} = 1.2745 cm

Partial Results

#	name	E_{in} (MeV/u)	E_{out} (MeV/u)	E_{loss} (MeV)	σ_E (MeV/u)	σ_{pos} (cm)	σ_a (mrad)	range (g/cm^2)	σ_r (g/cm^2)	dE_{in}/dx (MeV/(g/cm^2))	tof (ns)	Reaction rate
0	Air	101.592	99.297	2.311	0.178	1.254	7.12	9.097	0.102	6.34	23.253	0.005
1	E18 plastic set up	99.297	86.834	12.553	0.413	0.014	14.962	7.75	0.086	7.24	0.128	0.003
2	E18 trigger plate	86.834	80.936	5.941	0.265	4.437e-3	10.923	6.098	0.068	8.01	0.059	0.001
3	Plastic Fiber Layer 1	80.936	79.19	1.759	0.139	7.168e-4	6.105	5.376	0.061	8.452	0.017	0.000
4	Dark Box	79.19	76.349	2.862	0.184	6.386e-4	10.915	6.313	0.074	7.11	8.666e-3	0.001
5	Plastic Fiber Layer 2	76.349	74.521	1.842	0.138	7.587e-4	6.465	4.841	0.055	8.84	0.018	0.000
6	Sputtering	74.521	74.506	0.015	0.013	2.373e-7	0.804	5.666	0.067	7.445	4.415e-5	0.000
7	Plastic Fiber Layer 3	74.506	72.642	1.877	0.138	7.770e-4	6.622	4.633	0.053	9.008	0.018	0.000
8	Plastic Fiber Layer 4	72.642	70.741	1.915	0.138	7.964e-4	6.79	4.427	0.05	9.186	0.018	0.000

Figure 10.2: Calculation of the energy loss for the pions. [25]

10.1.2 Protons (p=310MeV/c)

Matter

#	name	matter	density (g/cm^3)	thick. (mg/cm^2)	thick. (cm)
0	Air	Air	0.001205	361.5	300
1	E18 plastic set up	BC_400	1.032	412.8	0.4
2	E18 trigger plate	BC_400	1.032	722.4	0.7
3	Plastic Fiber Layer 1	BC_400	1.032	206.4	0.2
4	Dark Box	Al2O3	3.97	397	0.1
5	Plastic Fiber Layer 2	BC_400	1.032	206.4	0.2
6	Sputtering	Al2O3	3.97	1.99	5.0000e-4
7	Plastic Fiber Layer 3	BC_400	1.032	206.4	0.2
8	Plastic Fiber Layer 4	BC_400	1.032	206.4	0.2

Figure 10.3: Left: Values for the material, the protons with 310 MeV/c and 322 MeV/c had to pass. The thickness of the E18-Setup was lower than for the pion run. The sputtering again had no relevant part, therefore it appears in the list only in one place to illustrate the minor role. [25]

Total Results

Projectile: 1H @ 49.5247MeV/u Change

E_{out} = 0.0000 MeV/u E_{loss} = 49.885 MeV σ_a = 0 mrad Reaction rate: N/A

$B\varrho$ = 0.00000 Tm σ_E = 0 MeV/u σ_{pos} = 2.5729 cm

β = 0.00000 TOF = 32.754812 ns

Partial Results

#	name	E_{in} (MeV/u)	E_{out} (MeV/u)	E_{loss} (MeV)	σ_E (MeV/u)	σ_{pos} (cm)	σ_a (mrad)	range (g/cm^2)	σ_r (g/cm^2)	dE_{in}/dx (MeV/(g/cm^2))	tof (ns)	Reaction rate
0	Air	49.525	45.436	4.118	0.178	2.546	14.684	2.513	0.03	11.017	32.527	0.007
1	E18 plastic set up	45.436	39.691	5.788	0.202	3.644e-3	15.955	1.895	0.022	13.303	0.046	0.001
2	E18 trigger plate	39.691	27.513	12.266	0.297	0.01	26.784	1.482	0.018	14.829	0.089	N/A
3	Plastic Fiber Layer 1	27.513	23.143	4.402	0.144	2.126e-3	18.802	0.76	9.338e-3	19.931	0.029	N/A
4	Dark Box	23.143	14.496	8.71	0.22	2.318e-3	44.313	0.701	9.162e-3	18.57	0.017	N/A
5	Plastic Fiber Layer 2	14.496	4.45	10.119	0.265	4.594e-3	53.485	0.235	2.995e-3	34.088	0.047	N/A
6	Sputtering	4.45	4.314	0.137	0.012	3.865e-6	13.188	0.039	5.374e-4	68.165	1.725e-4	N/A
7	Plastic Fiber Layer 3	4.314	0	4.346	0	7.881e-4	0	0.027	3.552e-4	92.195	0	N/A
8	Plastic Fiber Layer 4	0	0	0	0	0	0	0	0	0	0	0.000

Figure 10.4: Calculation of the energy loss for protons (p=310MeV/c). [25]

10.1.3 Protons (p=322MeV/c)

Total Results

Projectile: 1H @ 53.327MeV/u Change

E_{out} = 0.0000 MeV/u E_{loss} = 53.7151 MeV σ_a = 0 mrad Reaction rate: N/A

Bϱ = 0.00000 Tm σ_E = 0 MeV/u σ_{pos} = 2.3874 cm

β = 0.00000 TOF = 31.591828 ns

Partial Results

#	name	E_{in} (MeV/u)	E_{out} (MeV/u)	E_{loss} (MeV)	σ_E (MeV/u)	σ_{pos} (cm)	σ_a (mrad)	range (g/cm^2)	σ_r (g/cm^2)	dE_{in}/dx (MeV/(g/cm^2))	tof (ns)	Reaction rate
0	Air	53.327	49.488	3.867	0.177	2.363	13.588	2.871	0.034	10.392	31.353	0.006
1	E18 plastic set up	49.488	44.166	5.361	0.2	3.336e-3	14.53	2.213	0.026	12.425	0.044	0.001
2	E18 trigger plate	44.166	33.314	10.931	0.286	8.939e-3	23.223	1.8	0.021	13.609	0.083	0.001
3	Plastic Fiber Layer 1	33.314	29.649	3.692	0.141	1.739e-3	15.162	1.078	0.013	17.084	0.026	N/A
4	Dark Box	29.649	23.034	6.663	0.197	1.746e-3	31.513	1.092	0.014	15.305	0.014	N/A
5	Plastic Fiber Layer 2	23.034	17.807	5.265	0.15	2.578e-3	23.304	0.549	6.822e-3	23.055	0.032	N/A
6	Sputtering	17.807	17.762	0.045	0.012	9.661e-7	3.272	0.438	5.845e-3	22.899	8.648e-5	N/A
7	Plastic Fiber Layer 3	17.762	10.645	7.169	0.173	3.488e-3	33.738	0.341	4.297e-3	28.683	0.039	N/A
8	Plastic Fiber Layer 4	10.645	0	10.722	0	3.471e-3	0	0.134	1.734e-3	44.314	0	N/A

Figure 10.5: Calculation of the energy loss for protons (p=322MeV/c). The material did not change in comparison to protons with p=310MeV/c. [25]

Bibliography

[1] Cern. Cosmic rays: particles from outer space. [Online]. Available: https://home.cern/science/physics/cosmic-rays-particles-outer-space

[2] P. Biermann and G. Sigl, "Introduction to cosmic rays," in *Physics and Astrophysics of Ultra-High-Energy Cosmic Rays*. Springer, 2001, pp. 1–26.

[3] F. Halzen, "Pionic photons and neutrinos from cosmic ray accelerators," *Astroparticle Physics*, vol. 43, pp. 155–162, 2013.

[4] J. Simpson, "Elemental and isotopic composition of the galactic cosmic rays," *Annual Review of Nuclear and Particle Science*, vol. 33, no. 1, pp. 323–382, 1983.

[5] M. Losekamm, S. Paul, and T. Pöschl, "The radmap telescope on the international space station," 2020.

[6] A. Olinto, "The origin of the highest energy cosmic rays," in *Relativistic Aspects Of Nuclear Physics*. World Scientific, 2001, pp. 38–57.

[7] M. Losekamm, M. Milde, T. Pöschl, D. Greenwald, and S. Paul, "A new analysis method using bragg curve spectroscopy for a multi-purpose active-target particle telescope for radiation monitoring," *Nuclear Instruments and Methods in Physics Research Section A: Accelerators, Spectrometers, Detectors and Associated Equipment*, vol. 845, pp. 520–523, 2017.

[8] W. Demtröder, *Experimentalphysik 4*. Springer, 2005.

[9] G. F. Knoll, *Radiation Detection and Measurment*, 3rd ed., 2000.

[10] M. Losekamm, T. Pöschl, D. Greenwald, and S. Paul, "Scintillator-based radiation monitors," Technical University of Munich, 2000.

[11] C. D'Ambrosio, "A short overview on scintillators," Cern, 2005.

[12] L. Kuraray Co. [Online]. Available: https://www.kuraray.com/uploads/5a717515df6f5/PR0150_psf01.pdf

[13] W. Riegler. Solid state detectors. Cern. [Online]. Available: http://riegler.web.cern.ch/lectures/lecture5.pdf

[14] S. Hunklinger, *Festkörperphysik*. Oldenbourg Verlag, 2009.

[15] D. Renker and E. Lorenz, "Advances in solid state photon detectors," p. P04004, 2009.

[16] H. Kolanoski and N. Wermes, *Teilchendetektoren*. Springer, 2016.

[17] K. GmbH, *KETEK Microcell Technology*, 2020. [Online]. Available: https://www.ketek.net/sipm/technology/microcell-construction/

[18] C. Gruhn, M. Binimi, R. Legrain, R. Loveman, W. Pang, M. Roach, D. Scott, A. Shotter, T. Symons, J. Wouters *et al.*, "Bragg curves pectroscopy," *Nuclear Instruments and Methods in Physics Research*, vol. 196, no. 1, pp. 33–40, 1982.

[19] S. Grdanovska, "Characterization of radiation damage to a novel photonic crystal sensor," Ph.D. dissertation, 2015.

[20] B. M. Lotz, "Treatment procedure and light output analysis of scintillating fibers for scintillating fiber trackers."

[21] M. F. L'Annunziata, "Radiation physics and radionuclide decay," in *Handbook of Radioactivity Analysis*. Elsevier, 2012, pp. 1–162.

[22] K. GmbH, *Product Data Sheet SiPM – Silicon Photomultiplier*, 2020. [Online]. Available: https://www.ketek.net/wp-content/uploads/2018/12/KETEK-PM3325-WB-D0-Datasheet.pdf

[23] T. Orita, M. Uenomachi, and K. Shimazoe, "Development of time-over-threshold asics for radiation sensors." [Online]. Available: https://indico.cern.ch/event/669866/contributions/3227838/attachments/1770723/2877198/Poster_ToTASIC_181204.pdf

[24] A. Neiser, J. Adamczewski-Musch, M. Hoek, W. Koenig, G. Korcyl, S. Linev, L. Maier, J. Michel, M. Palka, M. Penschuck *et al.*, "Trb3: a 264 channel high precision tdc platform and its applications," *Journal of Instrumentation*, vol. 8, no. 12, p. C12043, 2013.

[25] A. Prochazka. [Online]. Available: https://www.isotopea.com/webatima/about.html

[26] K. and Tanabashi, M andd Hagiwara, K. Nakamura, K. Hikasa, M. Aguilar-Benitez, C. Amsler, R. Barnett, O. Dahl, D. Groom, R. Miquel *et al.*, 2018.